Geol. Mag. **155** (*8*), *2018, pp. 1705–1726.* © *Cambridge University Press 2017*

doi:10.1017/S001675681700067X

REE partition among zircon, orthopyroxene, amphibole and garnet in a high-grade metabasic system

ANNAMARIA FORNELLI*†, ANTONIO LANGONE‡, FRANCESCA MICHELETTI* & GIUSEPPE PICCARRETA*

*Earth Science and Geo-environmental Department, "Aldo Moro" Bari University via E. Orabona, 4-70125 Bari, Italy
‡Institute of Geosciences and Earth Resources (CNR) - U.O.S. of Pavia, via Ferrata, 1-27100 Pavia, Italy

(*Received* 30 November 2016; *accepted* 14 July 2017; *first published online* 24 August 2017)

Abstract – A mafic amphibole-bearing granulite with porphyroblastic garnet was investigated to evaluate: (1) the rare earth element (REE) partition among garnet, zircon, orthopyroxene and amphibole during the metamorphic evolution; (2) the significance of the REE distribution along lobes and bights of reabsorbed garnet rim; and (3) REE distribution coefficient values (DREE) suggestive of chemical equilibrium, assuming garnet as a reference. The results have been compared with those deriving from an intermediate granulite containing porphyroblastic garnet, without amphibole. Porphyroblastic garnet from both samples is rimmed by a continuous corona formed during post-peak decompression characterized by REE-enriched lobes and REE-poor bights. The amphiboles from corona have various REE abundances, reflecting a different dissolution rate of original garnet rim. The initial slow rate of garnet dissolution caused high REE concentration in the new garnet rim due to intra-crystalline diffusion, leading to the formation of REE-poorer amphiboles in corona. Subsequently, under an increasing geothermal gradient and fluid-present conditions, the faster dissolution of garnet determined the formation of bights and the transfer of REEs towards the corona. The timing of garnet growth and its dissolution were checked by U–Pb zircon ages. The zircons dated from 339 Ma to 303 Ma in two rock types combined with the garnet domains (core, outer core, rim) show similar distribution of patterns relative to heavy rare earth elements for zircon and garnet ($DHREE_{zrn/grt}$), suggesting chemical equilibrium. Zircons dated at *c.* 300 Ma do not appear in equilibrium with REE-rich garnet lobes, and younger zircons (278 Ma) show a new equilibrium with REE-poor garnet bights. On this basis, the $DHREE_{amph/grt}$ values obtained in specific textural sites might be interpreted as suggestive of equilibrium under granulite conditions.

Keywords: mafic granulites, REE in garnet, zircon, orthopyroxene, amphibole, U–Pb zircon ages, southern Italy

1. Introduction

A multidisciplinary methodological approach, including petrographic investigations, mineral and bulk-rock chemistries and U–Pb zircon geochronology, allows the age, origin and metamorphic evolution of lower crust sectors to be unravelled. Petrological studies of metamorphic paragenesis constrain the mineral equilibrium by taking into account the major-element distribution among principal mineral phases. On the other hand, the distribution of rare earth elements (REEs) among pairs of minerals such as garnet, zircon, orthopyroxene and amphibole during the high-grade metamorphism and anatexis, together with zircon geochronology, is one of the most challenging applications to define the chemical equilibrium among mineral phases and to constraint the ages of events in high-grade polyphasic metamorphic terranes. Well-constrained pressure–temperature–time (*P-T-t*) paths of lower crust sectors are useful for calculating the REE distribution coefficients (DREE) between competitors and for determining the DREE values indicative of chemical equilibrium. The paper provides middle to heavy rare earth element distribution coefficients between opportune competitors indicative of chemical equilibrium, derived from a petrological study based on textural relationships, geothermobarometric calculations and geochronological data.

Under granulite-facies conditions, the influence of temperature, pressure, rock chemistry and aqueous fluids or melts (open or closed system) on the magnitude of the equilibrium distribution coefficients of the REE is still to be proved. More data on rare earth element distribution coefficients between mineral phases in competition can help to identify equilibrium mineral assemblage pertinent to each metamorphic stage.

The distribution of REEs among pairs of minerals such as garnet, zircon and orthopyroxene has been investigated in natural and experimental examples producing a wide data range. Few data concerning the REE distribution between amphibole and garnet are currently available (Storkey *et al.* 2005; Zong *et al.* 2010).

The majority of the empirical data refers to zircon–garnet pairs (Harley *et al.* 2001; Rubatto, 2002; Whitehouse & Platt, 2003; Harley & Kelly, 2007; Buick

†Author for correspondence: annamaria.fornelli@uniba.it

et al. 2006) in pelitic systems equilibrated under typical granulite-facies conditions (i.e. 750–900 °C and 0.6–1.2 GPa).

Only two significant experiments for REE distribution between zircon and garnet were performed. However, they relate to examples equilibrated under different pressures and containing either garnet with high Ca contents (10–22 wt % in Rubatto & Hermann, 2007) or without Ca (Taylor *et al.* 2015). The combinations of empirical and experimental data led to two hypotheses: (1) the REE distribution defines a flat pattern with values around unity (Harley *et al.* 2001; Whitehouse & Platt, 2003; Hokada & Harley, 2004; Kelly & Harley, 2005; Harley & Kelly, 2007; Taylor *et al.* 2015) regardless of temperature (Taylor *et al.* 2015); or (2) the REE distribution defines steep positive patterns with an increase of DREE values under lowering temperature (up to 800 °C), favouring zircon with respect to garnet (Rubatto, 2002; Hermann & Rubatto, 2003; Buick *et al.* 2006; Rubatto & Hermann, 2007). Empirical REE distribution coefficients in the zircon–garnet pairs from an intermediate, amphibole-free granulite (GRT3) were calculated by Fornelli *et al.* (2014). The resulting equilibrium values differ significantly from other empirical data, being on average $D_{Gd\text{-}Ho}<1$ ($D_{Gd} = 0.18$; $D_{Ho} = 0.53$) and $D_{Tm\text{-}Lu}>1$ ($D_{Tm} = 1.37$; $D_{Lu} = 3.12$); only the D_{Er} value is around unity (0.89). Regarding the REE distribution between orthopyroxene and garnet coexisting with zircon, Harley *et al.* (2001) proposed $DHREE_{opx/grt}$ values (abbreviations of minerals according to Kretz, 1983) suggestive of equilibrium in natural examples as lying within the range 0.03–0.01 under granulite-facies conditions. Fornelli *et al.* (2014) observed a wider variation of DREE values for coexisting orthopyroxene and garnet during granulite-facies metamorphism. Whether the DREE values are indicative of equilibrium or not remains an unresolved question.

An effective competitor for medium REE (MREE) and heavy REE (HREE) with zircon, garnet and orthopyroxene is amphibole (Skublov & Drugova, 2003), which can be consumed or formed during the prograde and retrograde stages in mafic or intermediate granulites (Storkey *et al.* 2005). The HREE competition between amphibole and garnet is documented in some mafic and intermediate granulites (Storkey *et al.* 2005; Buick *et al.* 2006; Zong *et al.* 2010), but the role of zircon in the HREE partition has not been discussed. An evaluation of the empirical REE distribution between amphibole and garnet can therefore indicate equilibrium DREE values, taking into account the deductions of calculated DREE values relative to zircon–garnet and orthopyroxene–garnet pairs for which an assessment of the equilibrium was made.

In this study a mafic amphibole-bearing granulite (Tur76A) has been considered for the REE distribution among zircon, orthopyroxene and amphibole with respect to garnet. Calculated data are compared with those of the intermediate granulite (GRT3) already studied by Fornelli *et al.* (2014). The rock types experienced the same physical conditions ($700<T<900$ °C and $0.7<P<1.0$ GPa) and contain garnet with similar grossular content (about 16 %) and zircon grains with core-rim structures. The dating of zircons, the REE contents of zircon, garnet, orthopyroxene, amphibole and the reconstructed metamorphic *P-T-t* path (Fornelli *et al.* 2011; Fornelli, Pascazio & Piccarreta, 2011) yield information about the DREE values suggestive of equilibrium between the above phases in the considered chemical systems.

2. Geological setting

A pile of crystalline rocks (Fig. 1), stacked during the Alpine orogenesis *sensu lato*, crops out in southern Italy (Amodio Morelli *et al.* 1976). The uppermost nappe (Sila Unit) consists of (from the bottom to the top): (1) a 7–8 km thick slice of lower-crust rocks (Schenk, 1980; Fornelli *et al.* 2004); (2) a *c.* 13 km thick 'layer' of granitoids (Caggianelli, Prosser & Rottura, 2000; Fornelli *et al.* 2004); and (3) medium- to low-grade upper-crust metamorphic rocks. The lower-crust rocks in the Serre Massif include (from the bottom to the top; Fig. 1): (1) granulite-facies metagabbros and meta-monzogabbros with rare meta-peridotites, felsic granulites and metapelites; and (2) metapelites with intercalations of metabasites, rare marbles and felsic orthogneisses (Paglionico & Piccarreta, 1978; Schenk, 1984; Micheletti *et al.* 2007). U–Pb data on separate and *in situ* zircons (conventional and spot analyses) from mafic and felsic metaigneous rocks at the base and top of the lower-crust portion yield late Neoproterozoic – early Cambrian ages (545–575 Ma) for the emplacement of their igneous protoliths (Schenk, 1989; Micheletti *et al.* 2007, 2008; Fornelli *et al.* 2011). Metagabbros occur within the felsic granulites at the bottom of the section and concordant layers of metabasites are interleaved with the adjacent felsic granulites and metapelites (Fig. 1). Multistage decompression coupled with partial melting has been documented in the metagabbros of the lower crust on the basis of microtextural evidence and thermobarometric data (Fornelli *et al.* 2011; Fornelli, Pascazio & Piccarreta, 2011). The resulting assemblage reflects local variation of H_2O activity, as evidenced by the formation of Pl-Opx, Pl-Opx-Am or Pl-Am coronas around clinopyroxene and porphyroblastic garnet (e.g. Schenk, 1984; Caggianelli *et al.* 1991; Fornelli *et al.* 2002; Acquafredda *et al.* 2006, 2008). The granulite-facies rocks contain amphibole and plagioclase as relicts of the pre-granulite metamorphic stages (e.g. Paglionico & Piccarreta, 1976; Maccarrone *et al.* 1983; Schenk, 1984; Acquafredda *et al.* 2008). In Figure 1c, the clockwise *P-T* trajectory related to Variscan metamorphism reconstructed by Acquafredda *et al.* (2006, 2008), implies: (1) *P-T* estimates of 1.1 GPa and *c.* 900 °C dated at 347–340 Ma (zircon ages in Fornelli *et al.* 2011 and Sm–Nd age of garnet in Duchene *et al.* 2013) at the metamorphic peak forming granulite assemblage

https://doi.org/10.1017/S001675681700067X Published online by Cambridge University Press

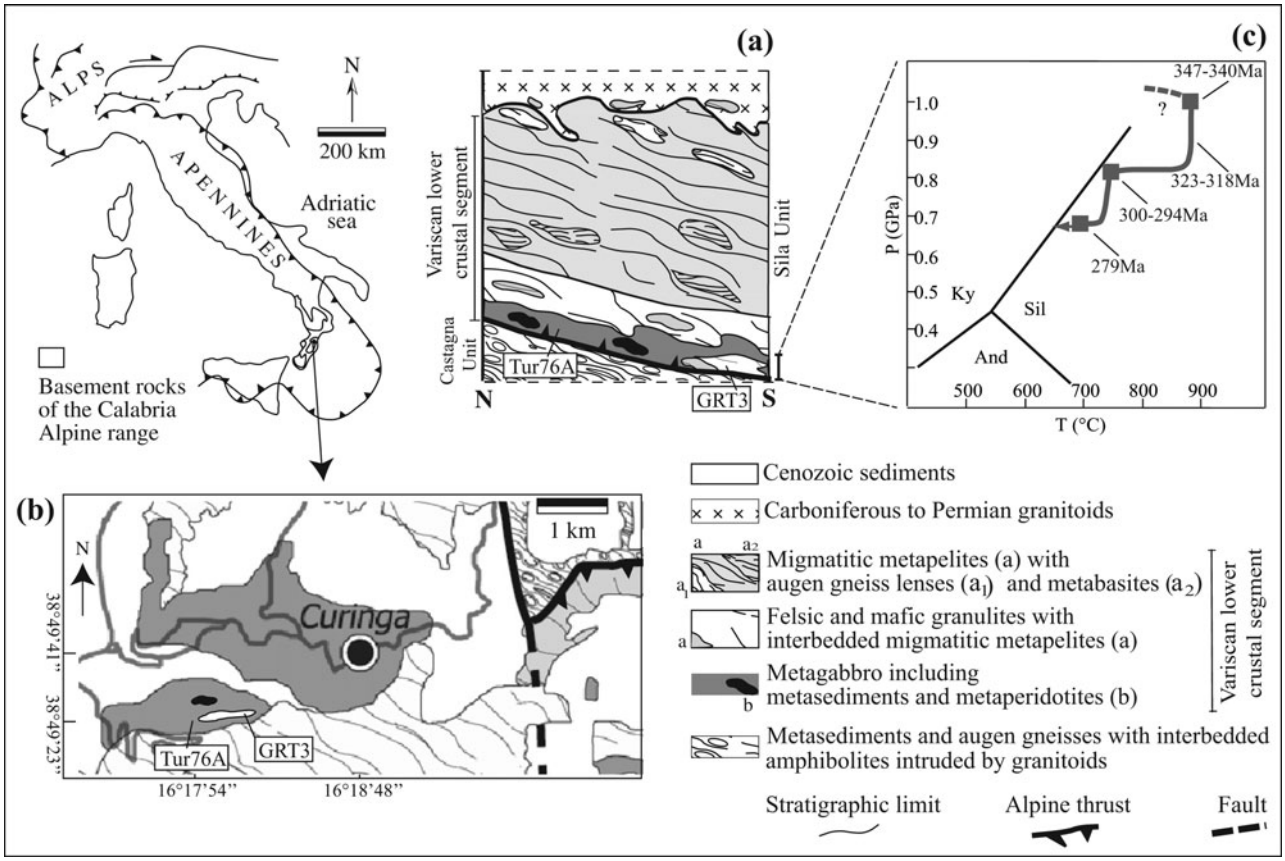

Figure 1. (a) Map of Italy and schematic stratigraphic section of the Hercynian lower crust, not to scale. (b) Geological map of the sampled area from Fornelli *et al.* (2011). (c) *P-T-t* path of the lower portion of the studied deep crust from Fornelli *et al.* (2011).

(garnet, clinopyroxene and orthopyroxene); (2) decompression at 0.8–0.9 GPa and 850 °C testified by a corona formed by orthopyroxene-plagioclase ± amphibole dated at 323–318 Ma between clinopyroxene and garnet; and (3) a further decompression and cooling stage at *c.* 300 Ma at *P* of 0.7–0.8 GPa and *T* of 650–750 °C completed at 279 Ma (zircon age in garnet-bearing metagabbros) (Fornelli, Pascazio & Piccarreta, 2011; Fornelli *et al.* 2012). During the last decompression (from 300 Ma until 279 Ma) a symplectitic corona including hydrous minerals and consisting of orthopyroxene, plagioclase, amphibole and biotite formed around the porphyroblastic garnets in the mafic and intermediate metamorphic rocks (Acquafredda *et al.* 2008; Fornelli *et al.* 2014). The studied sample (Tur76A) derives from the lower part of the Serre deep crust (latitude 38 °49′ 23″ N, longitude 16° 17′ 54″ E). The previously studied sample GRT3 with which Tur76A is compared (Fornelli *et al.* 2014) derives from the same crust level. In both samples porphyroblastic garnet is surrounded by symplectitic corona formed during the last decompression stages. New empirical REE distribution coefficients between zircon/garnet and orthopyroxene/garnet have been calculated in the sample Tur76A and compared with those of both sample GRT3 and data in the literature to infer the equilibrium conditions; these were then utilized to calculate for the first time the REE distribution coefficients between coexistent amphibole and garnet under granulite-facies conditions.

3. Analytical methods

Chemical compositions of the whole rocks and major-element compositions in garnet, orthopyroxene, amphibole and biotite were performed at Bari University by x-ray fluorescence (XRF) spectrometry and a Cambridge S360 electron microscope equipped with a LINK AN 10.000 Si (Li) energy dispersive detector.

Trace-element composition was collected on specific domains of zircon, garnet, orthopyroxene and amphibole in the different textural sites; in addition, trace-element core-rim profiles relative to the porphyroblastic garnets were performed. These analyses were performed by laser ablation inductively coupled plasma mass spectrometry (LA-ICP-MS) (CNR, Istituto di Geoscienze e Georisorse Unità di Pavia, Italy). This instrument couples a Nd:YAG (neodymium-doped yttrium aluminium garnet) laser working at 266 nm with a quadrupole ICP mass spectrometer of type DRCe from Perkin Elmer. For trace-element determinations the laser was operated at a repetition rate of 10 Hz, with pulse energy *c.* 0.01 mJ and an ablation spot of *c.* 25 μm in size. For the acquisition of parameters, the reader is referred to Tiepolo *et al.* (2002). NBS NIST-610 was adopted as an external standard;

https://doi.org/10.1017/S001675681700067X Published online by Cambridge University Press

precision and accuracy were assessed on the BCR-2 USGS reference glass and are better than 6 % relative (see online supplementary Table S1, available at http://journals.cambridge.org/geo). Different major elements were adopted as internal standards: ^{29}Si for orthopyroxene and zircon and ^{44}Ca for garnet, amphibole and clinopyroxene. Data reduction was carried out using the GLITTER software package (van Achterbergh *et al*. 2001). Minimum detection limits at 99 % confidence level were $<10^{-5}$ ppm for most of the trace elements.

External morphology and internal microtextures of zircon on thin-section were observed by scanning electron microscropy (SEM) using a Zeiss EVO50XVP SEM (Bari University, Italy) equipped with a variable-pressure secondary-electron (VPSE) detector in high vacuum conditions (Griffin, Joy & Michael, 2010). This technique gives high-resolution images revealing the internal structures of zircon. In the sample Tur76A observations were made on seven separated zircon grains and five crystals in thin-section. The most suitable sites for spot analyses were selected on the images. All zircon grains were inspected before and after the isotopic and trace-element analyses in order to check the precise location of the spots.

Age determinations at IGG-CNR (Pavia, Italy) were performed using a 193 nm ArF excimer laser ablation (LA) microprobe (GeoLas200QMicrolas) coupled with a magnetic sector ICP-MS (Element 1 from Thermo Finnigan). The U–Pb analyses were carried out in single spot mode and with a spot size of *c.* 10 μm or 20 μm depending on crystal size. The laser operated at a frequency of 5 Hz and with a fluence of 12 J cm^{-2}. Sixty seconds of background signal and at least 30 s of ablation signal were acquired. The signals of masses ^{202}Hg, ^{204}(Pb + Hg), ^{206}Pb, ^{207}Pb, ^{208}Pb, ^{232}Th and ^{238}U were acquired in magnetic scan mode. ^{235}U is calculated from ^{238}U on the basis of the ratio ^{238}U/^{235}U = 137.88. The 202 and 204 masses were collected in order to monitor the presence of common Pb in zircon. In particular, the signal of ^{202}Hg was acquired to correct the isobaric interference of ^{204}Hg on ^{204}Pb (Horn, Rudnik & McDonough, 2000). The relatively high-Hg background prevents the detection of low ^{204}Pb signals, however, hampering the calculation of small common Pb contributions. In the present work all analysed zircons have shown signals of 204 mass indistinguishable from the background; as a result, no common Pb correction has been applied (more analytical details in Tiepolo, 2003). Mass bias and laser-induced fractionation were corrected by adopting zircon 91500 (1062.4 ± 0.4 Ma; Wiedenbeck *et al.* 1995) as the external standard. During each analytical run, reference zircon 02123 (295 Ma; Ketchum *et al*. 2001) was analysed together with unknowns (see online supplementary Table S2, available at http://journals.cambridge.org/geo) for quality control; the resulting ages were 293 ± 10 Ma (Oc12a) and 293 ± 6 Ma (Oc12b). Time-resolved signals were carefully inspected to detect perturbation of the signal related to inclusions, cracks or mixed age domains. Within the same analytical run, the error associated with the reproducibility of the external standards was propagated to each analysis of the sample (see Horstwood *et al.* 2003); after this procedure, each age determination is considered accurate within the quoted error. The concordia test was performed for each analytical spot from ^{206}Pb/^{238}U and ^{207}Pb/^{235}U ratios using the relevant function in the software package Isoplot/Ex3.00 (Ludwig, 2003). The same software was used to calculate the mean concordia age and the mean square of weighted deviates (MSWD). The percentage of discordance is calculated as {[1–(^{206}Pb/^{238}U age/^{207}Pb/^{235}U age)]×100}. U–Pb ages are considered as concordant for a percentage of discordance within the range ±1 %, whereas U–Pb ages are considered as sub-concordant for a percentage of discordance up to 3 %. Discordant data have not been taken into account.

4. Petrography and whole-rock chemistry

The studied sample (Tur76A) shows foliation defined by brown amphibole, plagioclase and orthopyroxene; accessory minerals are apatite, zircon and Fe-oxide. The porphyroblastic garnet (2 cm in size) includes amphibole, plagioclase, orthopyroxene and drop-like quartz (Fig. 2a). Many small crystals of zircon are present within and around the garnet, which is surrounded by a continuous corona consisting of plagioclase, orthopyroxene, amphibole and biotite. One clinopyroxenitic nodule is separated from the near-porphyroblastic garnet by a corona of amphibole, orthopyroxene and plagioclase (Fig. 2a).

With the exception of the presence of amphibole, this sample shows features in common with the intermediate granulite (GRT3) derived from the same crust level (Fornelli *et al.* 2014). The common features are (Fig. 2): (1) the elongated shape of garnet rimmed by symplectitic corona formed by plagioclase, orthopyroxene and small flakes of biotite; and (2) the presence of a rim characterized by millimetric lobes and bights (Fig. 2a, insert bottom right). Symplectitic corona around garnet is continuous and both lobes and bights have been considered as steps of the dissolution of the original garnet rim during the progressive decompression (Fornelli *et al.* 2014). In this sample the multistage decompression (Fig. 1c) is evidenced by the corona around the clinopyroxenite nodule dated at 323–318 Ma in Acquafredda *et al*. (2008) and by the symplectite around garnet formed during 300–279 Ma (Fornelli *et al*. 2011).

The sample (Tur76A) has a gabbroic composition with Mg number [MgO/(MgO + FeO)×100] = 39, SiO_2 = 49.19 wt % and K_2O = 0.65 wt % (Table 1). The REE pattern is poorly differentiated (Fig. 3) with relative enrichment of LREE with respect to HREE without Eu anomaly (La_N/Lu_N ratio = 2.71; ΣLREE = 65.84 ppm; ΣHREE = 18.37 ppm; Eu/Eu* = 0.93).

https://doi.org/10.1017/S001675681700067X Published online by Cambridge University Press

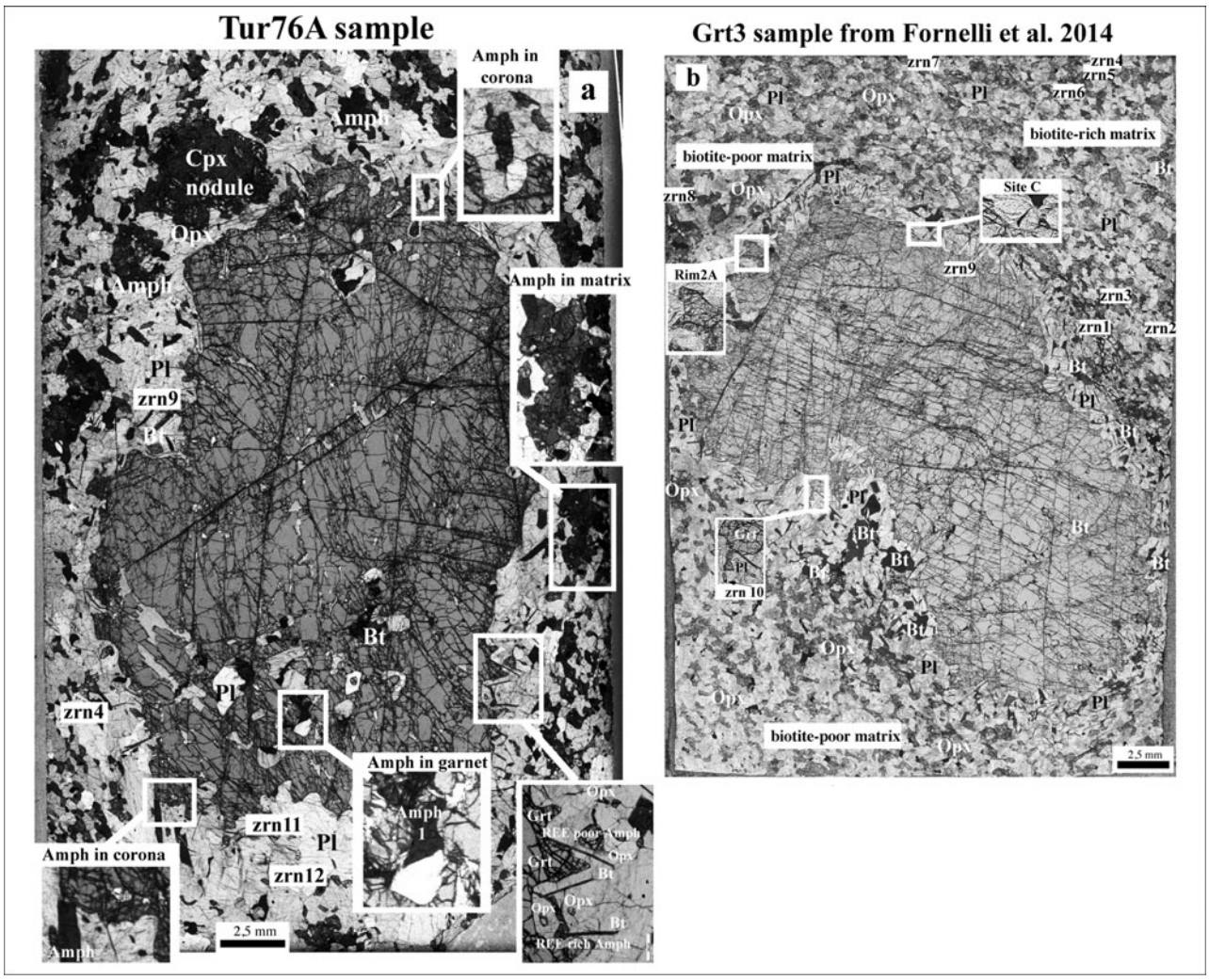

Figure 2. Microphotographs of thin-sections showing porphyroblastic garnets and locations of zircon (zrn), biotite (Bt), orthopyroxene (Opx), plagioclase (Pl), clinopyroxene (Cpx) and amphibole (Amph). (a) Sample Tur76A; REE-rich amphibole and REE-poor amphibole in bight and lobe of garnet, respectively, are indicated in insert at the bottom on the right. (b) Sample GRT3 modified from Fornelli *et al.* (2014). Abbreviations of minerals according to Kretz (1983).

The comparison with the chemical composition of the intermediate granulite (GRT3 from Fornelli *et al.* 2014) shows that, despite the different major-element composition, the REE abundances are comparable in both samples even if the Tur76A sample shows a quite flat REE pattern without Eu anomaly and a slightly higher content of Nd, Sm, Gd, Tb and Dy (Table 1; Fig. 3).

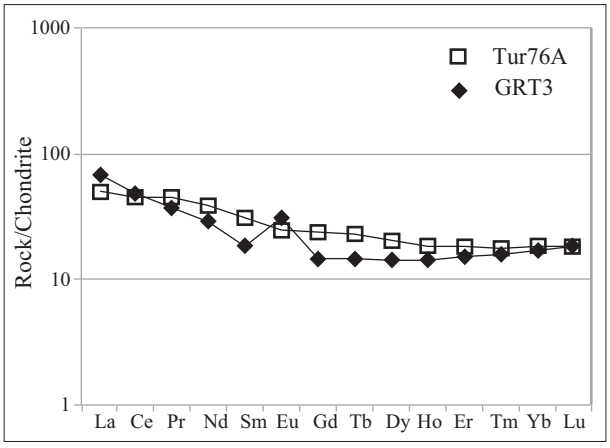

Figure 3. REE patterns of whole rocks nomalized to McDonough & Sun (1995) chondrite.

5. Mineral chemistry and U–Pb zircon ages

The U–Pb zircon ages and the chemical compositions of garnet, orthopyroxene, zircon, amphibole and biotite have been discussed and compared with those from sample GRT3 (Fornelli *et al.* 2014).

5.a. Sample Tur76A

Garnet is an almandine (50–57 mol %)-pyrope (19–25 mol %)-grossular (15–18 mol %) solid solution with minor andradite (4–5 mol %) and spessartine (3–4 mol %) components. Substantially, it shows a flat end-member profile with slight decrease of Mg number from the core (33) to the rim (28). The

https://doi.org/10.1017/S001675681700067X Published online by Cambridge University Press

Table 1. Chemical composition of whole rocks.

	GRT3	Tur76A
SiO_2	62.56	49.19
TiO_2	1.24	1.30
Al_2O_3	15.20	17.99
Fe_2O_3	8.28	10.64
MnO	0.11	0.17
MgO	3.22	6.07
CaO	4.82	10.15
Na_2O	2.93	3.42
K_2O	0.54	0.65
P_2O_5	0.17	0.24
LOI	0.38	0.19
Mg-number	30	39
ppm		
Ba	382	211
Rb	4	2
Sr	425	267
Y	23	30
Zr	433	109
Nb	11	6
V	146	178
Cr	101	190
Ni	43	61
Co	26	35
Ga	19	19
Hf	11	3
Pb	6	5
Ta	0.62	0.38
Th	0.52	0.32
La	15.98	11.79
Ce	30.05	27.68
Pr	3.41	4.24
Nd	13.07	17.63
Sm	2.68	4.50
Eu	1.72	1.40
Gd	2.94	4.73
Tb	0.53	0.81
Dy	3.48	5.04
Ho	0.78	1.01
Er	2.41	2.91
Tm	0.40	0.44
Yb	2.76	2.98
Lu	0.46	0.46
REE	80.67	85.62
Eu/Eu*	1.88	0.93

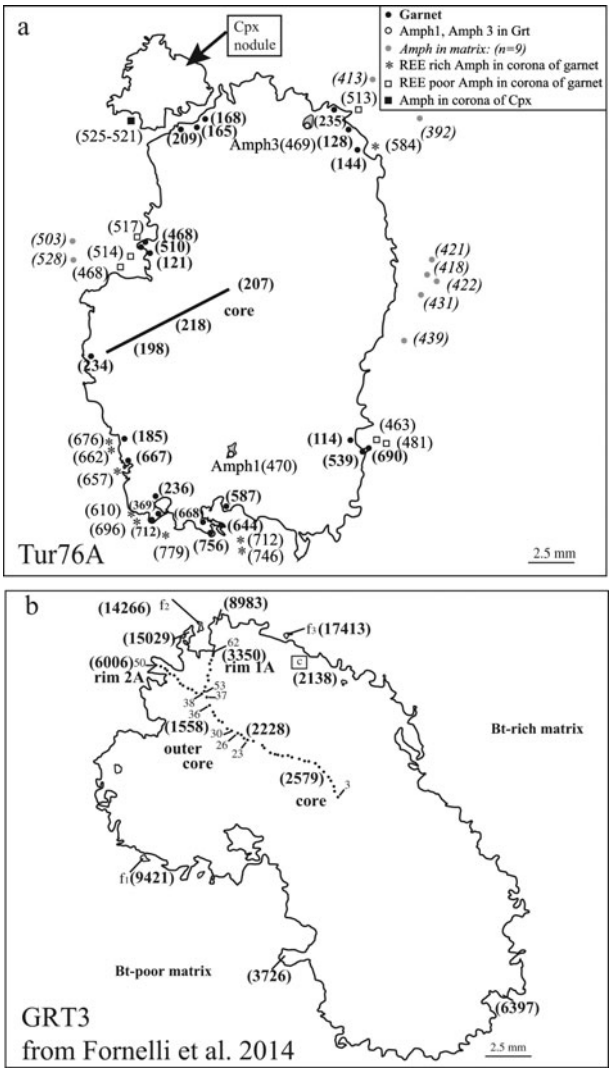

Figure 4. Sketches of thin-sections. (a) Analysed sites and ΣREE (in bold) of porphyroblastic garnet from (a) sample Tur76A and ΣREE (in brackets) of amphiboles in the different textural sites; and (b) sample GRT3 (numbers from 3 to 50 and from 53 to 62 represent the analyses along traverses from Fornelli *et al*. 2014).

edge of garnet demonstrates evidence of millimetric lobes and profound bights (Figs 2a, 4a) formed during the consumption of the original rim. The trace-element abundances (Table 2) and the REE patterns along a core–outer-core traverse (30 spot analyses) are homogeneous with variable ΣREE in the range 185–239 ppm (average 209 ppm), slight enrichment of HREE (Yb_N/Gd_N = 5.37; Fig. 5a) and small negative Eu anomaly (Eu/Eu^* = 0.68). Very different REE abundances occur along the present rim (Table 2; Figs 4a, 5a), where it is possible to observe: (1) a marked REE increase (up to 756 ppm; Fig. 4a) in the lobes with high Yb_N/Gd_N ratio (11.17) and low Eu/Eu^* value (0.36); and (2) a pronounced REE depletion at the bights (REE averaging 185 ppm) where REEs assume values comparable with those of garnet core (Fig. 5a), with lower Yb_N/Gd_N (average 5.25) and higher Eu/Eu^* (0.68) ratios.

Pyroxene is present as clinopyroxene in the clinopyroxenite nodule and as orthopyroxene in matrix and in coronas around the porphyroblastic garnet and the clinopyroxenite nodule.

The nodule consists of large crystals of diopside (En 33.8–38.5; Fs 15.4–19.2; Wo 45.5–47.8) with Mg number ranging from 81 (core) to 85 (rim). The REE contents of clinopyroxenes range from 168 ppm to 137 ppm with a negative Eu anomaly (Eu/Eu^* = 0.34) and a flat HREE pattern (Yb_N/Gd_N = 1.1) (Table 3; Fig. 6a).

The nodule is rimmed by corona formed by orthopyroxene, amphibole and plagioclase. The composition of orthopyroxene in this corona is En 52–56, Fs 43–46 with Mg number *c.* 60; amphibole is brown Fe-potassic pargasite with mg number *c.* 53 and plagioclase shows labradoritic composition with An_{53}.

Orthopyroxene included in garnet as well as that occurring in the symplectitic corona around the garnet are both Mg-rich (Mg number 62–66); orthopyroxene in matrix has a homogeneous chemical composition

https://doi.org/10.1017/S001675681700067X Published online by Cambridge University Press

Table 2. Trace elements (mean values in ppm and standard deviation σ) in core and rim (lobes and bights) of garnet from Tur76A sample. Details of analysed points in Figure 4a.

	Core		Rim lobes		Rim bights	
	$n = 30$	σ	$n = 10$	σ	$n = 15$	σ
Y	327	15	1023	159	318	128
Zr	–	–	18 ($n = 7$)	7	22 ($n = 7$)	2
Ti	672	120	377	121	596	177
Cr	74	13	107	67	81	17
V	124	4	243	29	128	22
Sc	53	3	157	22	123	61
Sr	0.17	0.12	0.24	0.17	0.38	1
Nb	0.02	0.05	0.03	0.04	0.03	0.08
Ba	0.09	0.08	0.07	0.09	0.13	0.14
La	0.03	0.03	0.03	0.07	0.03	0.04
Ce	0.31	0.13	0.18	0.10	0.19	0.11
Pr	0.18	0.06	0.11	0.03	0.15	0.07
Nd	2.49	0.40	2.06	0.77	2.22	0.56
Sm	3.60	0.58	5.87	1	3.92	2
Eu	1.60	0.16	1.48	0.37	1.50	0.32
Gd	14.40	1	28.12	8	13.60	4
Tb	4.59	0.32	9.84	2	4.26	1
Dy	44.39	2	112.64	25	41.40	14
Ho	12.82	0.88	35.77	7	11.72	4
Er	44.59	3	133.88	23	39.79	15
Tm	7.54	0.60	26.35	4	6.97	3
Yb	62.36	4	230.48	36	58.21	24
Lu	10.02	0.90	37.26	7	9.01	3
Hf	0.33	0.09	0.38	0.37	0.46	0.31
Th	0.01	0.02	0.01	0.02	0.02	0.03
U	0.02	0.01	0.01	0.01	0.01	0.01
ΣREE	209	12	624	94	193	69
ΣHREE	201	12	614	93	185	68
Yb_N/Gd_N	5.37	0.42	11.17	4	5.25	1
Eu/Eu^*	0.68	0.08	0.36	0.06	0.68	0.17

The analyses were performed by LA-ICP-MS (minimum detection limits at 99 % confidence level were $<10^{-5}$ for most of the elements; precision and accuracy were assessed on the BCR-2 USGS reference glass and are more than 6 % relative).

with Mg number *c.* 62 and low contents of REE (2–4 ppm), whereas crystals of corona around the clinopyroxenite nodule and garnet show homogeneously higher REE contents (Table 3; ΣHREE *c.* 8 ppm; Yb_N/Gd_N in the range 1.86–26.2; Y *c.* 10 ppm) (Fig. 6b). The homogeneous REE contents of orthopyroxene in the coronas of garnet and clinopyroxenite nodule could depend on the role of competitors such as amphibole and zircon and on the negligible influence of clinopyroxene.

Thirteen crystal domains were analysed for U–Pb isotopic system: eight crystals were separated and five grains were analysed *in situ* on thin-sections within symplectitic corona around garnet (Table 4, Fig. 2a). In Figure 7a, 13 concordant ages from 278 ± 6 Ma to 513 ± 9, two sub-concordant ages at 276 ± 6 Ma and 283 ± 10 Ma, and discordant data are represented. Zircon grains show core-rim textures (Fig. 7b) interpreted as indicating dissolution of the former crystal and successive precipitation forming the present rim (zrn 181; Fig. 7b). The younger ages from 278 ± 6 Ma to 345 ± 5 Ma (Table 4) represent 70 % of the analysed homogeneous luminescent domains, whereas the older ages (513 ± 9 Ma, 466 ± 15 Ma, 436 ± 15 Ma, 434 ± 6 Ma and 413 ± 6 Ma) are related to preserved/ghost oscillatory zoning inner domains (Fig. 7b).

Fourteen domains of zircons were analysed for trace elements (Table 5). The zircon age of two domains is unknown. The REE contents in the analysed zircons range from 146 ppm to 2516 ppm (Table 5). Generally, the older cores (413–513 Ma) are richer in Y, HREE, Sc and Pb and poorer in Li and U than the analysed younger zircon rims of age 278–303 Ma (Table 5, Fig. 8a). On the rim of zircon 181, dated at 303 Ma, three spot analyses were performed in order to verify its REE content. The average of the REE contents is 177 ppm (Table 5). The undated domain of zircon 215 shows low REE contents (242–297 ppm) as for the zircons dated at 303 Ma and 278 Ma (177 ppm and 363 ppm, respectively); it is therefore considered as a young zircon with an age in the range 278–303 Ma (Fig. 8a). On the whole, the analysed zircons show fractionated REE patterns (Yb_N/Gd_N from 31 to 56) with negative Eu anomalies decreasing in the younger domains (Eu/Eu^* ratio ranges from 0.29 to 1.0 in zircons with ages <303Ma) and positive Ce anomalies (Fig. 8a).

The lack of Eu negative anomaly together with the presence of positive Ce anomaly in zircons with ages 303 Ma and 278 Ma (Table 5) could be due to oxidizing conditions in the micro-domain favouring Eu^{+3} and Ce^{+4} rather than Eu^{+2} and Ce^{+3} (Trail, Watson & Tailby, 2012). In fact, the plagioclase preferentially

https://doi.org/10.1017/S001675681700067X Published online by Cambridge University Press

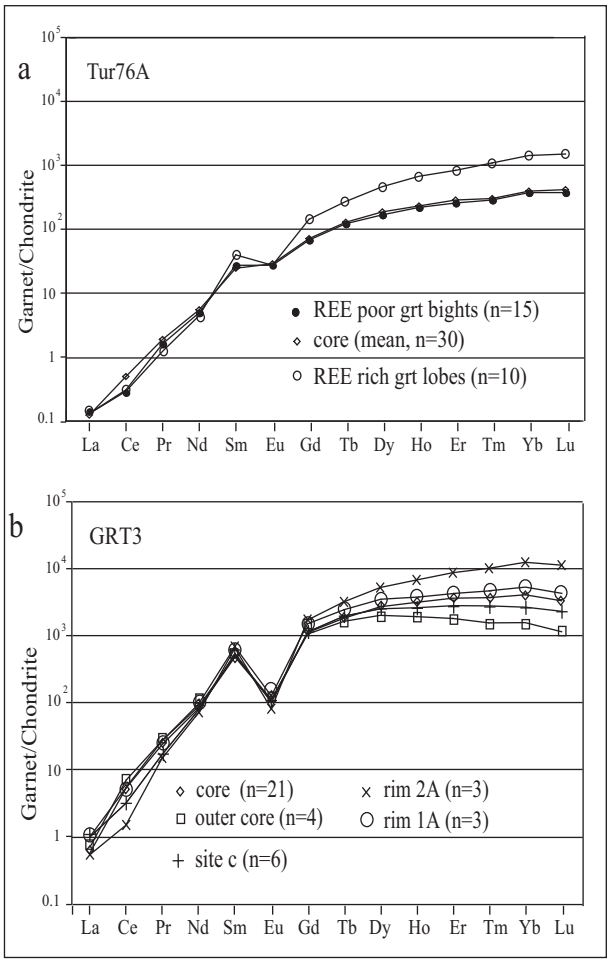

Figure 5. REE patterns in the different sites of porphyroblastic garnets normalized to chondrite (McDonough & Sun, 1995): (a) sample Tur76A and (b) sample GRT3 from Fornelli *et al.* (2014).

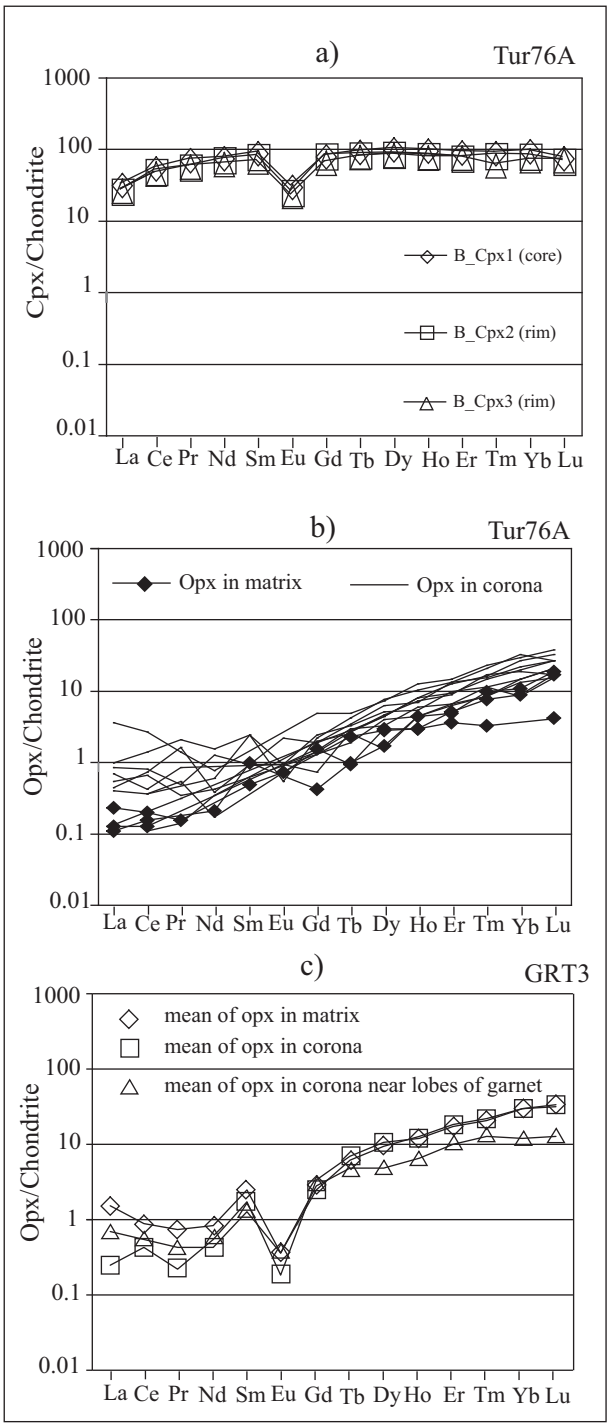

Figure 6. REE patterns of (a) clinopyroxenes in nodule, Tur76A sample; (b) orthopyroxene in corona and matrix, Tur76A sample; and (c) orthopyroxene in GRT3 sample (from Fornelli *et al.* 2014). REEs have been normalized to chondrite (McDonough & Sun, 1995).

incorporated Eu^{+2} in a reducing system inducing negative Eu anomaly in the other coexisting minerals. The last decompression in the studied rock occurred under fluid-present conditions after 303 Ma, causing the formation of a corona with plagioclase, amphibole, biotite, ±orthopyroxene and recrystallized zircons without Eu anomaly.

The Ti contents of zircons (generally from 8.6 ppm to 22 ppm) are unrelated to the ages. The Th/U ratio ranges from 0.09 to 0.44 with higher values in the older domains, suggesting a magmatic record (Xia *et al.* 2009; Chen, Zheng & Xie, 2010; Zhang, Zheng & Zhao, 2010). Zircon 11 in the symplectitic corona around garnet (Figs 2a, 7a; Table 5) deviates from the general behaviour since it shows a high value of Th/U (0.40) despite the younger age (278 ± 6 Ma); it might therefore have grown during the last decompression stage (dated at 280 Ma in Duchene *et al.* 2013) in a fluid- or melt-present context. Zircons with ages 413–513 Ma are richer in Y and HREE than the analysed younger zircons (278–303 Ma; Table 5; Fig. 8a).

Amphibole is present in garnet, matrix and coronas around the clinopyroxenite nodule and garnet. It is a brown Fe-potassic pargasite with K >0.36 atoms per formula unit (apfu). Major-element composition of amphibole in matrix, in garnet and in corona around clinopyroxenite nodule is homogeneous with Mg number *c.* 53 (Table 6). An increase of Mg number (54–60) characterizes the amphibole from symplectitic corona around garnet. Regarding the trace-element distribution (Table 7), amphibole included in the garnet core (amph 1 in Fig. 9; abbreviations of mineral according

https://doi.org/10.1017/S001675681700067X Published online by Cambridge University Press

Table 3. Trace elements (in ppm) of clinopyroxene in nodule and orthopyroxenes from corona and matrix (sample Tur76A).

	In corona							In matrix			In nodule		
	10-BOpx1	13-Bopx2	13-3opx1	14-3opx2	15-3opx3	08-2opx	10–3opx1	29-gOpx3	18-4opx2	19-4opx2	Cpx1	Cpx2	Cpx3
Y	9.56	4.08	14.1	15.23	10.79	7.90	9.11	3.42	5.43	4.89	116.49	107.93	92.98
Zr	–	–	6.79	1.5	0.59	1.92	0.81	–	1.23	0.93	–	–	–
Ti	553	328	463	805	367	692	477	517	466	445	2082	1894	1676
Cr	144	141	118	141	129	93	180	31	129	86	154	183	241
V	165	133	276	284	264	124	187	127	173	125	401	436	445
Zn	575	574	466	427	422	554	498	473	371	352	162	147	134
Sc	42	34	59	56	51	29	42	27	37	29	96	119	143
Sr	0.65	5.1	3.28	0	0.84	0.22	3.94	0.77	0.68	0.50	12.39	10.28	9.95
Nb	0.06	0.04	0.04	0.03	0.04	0	0	0	0	0.03	0.10	0.02	0.02
Ba	2.09	2.84	2.90	0.17	0.34	0.47	1.94	0.24	0.30	0.25	0.20	0.13	2.09
La	0.23	0.12	0	0.81	0.03	0.09	0.19	0.05	0.02	0.03	7.1	5.88	5.81
Ce	0.83	0.38	0.21	1.57	0	0.22	0.49	0.12	0.09	0.08	31.16	28.42	26.17
Pr	0.18	0.03	0	0.13	0.03	0.05	0.04	0.01	0	0	5.93	4.82	4.80
Nd	0.67	0.18	0.27	0.33	0	0.08	0.56	0	0.09	0	31.90	30.79	26.47
Sm	0.34	0	0.35	0	0	0	0.14	0.07	0.14	0	12.30	11.21	9.51
Eu	0.05	0	0.03	0	0	0	0.05	0.04	0	0	1.59	1.33	1.19
Gd	0.14	0	0.42	0.95	0.37	0	0.48	0	0.08	0.30	14.93	15.00	12.02
Tb	0.09	0.07	0.15	0.17	0.10	0.10	0.12	0.08	0.03	0.03	3.15	2.91	2.70
Dy	1.07	0.92	1.84	1.78	1.05	0.79	1.20	0.67	0.41	0.69	23.13	19.84	19.21
Ho	0.39	0.24	0.56	0.67	0.42	0.31	0.28	0.16	0.23	0.15	5.01	4.39	4.03
Er	1.39	0.99	2.04	2.27	1.98	1.03	1.51	0.55	0.74	0.80	13.49	11.50	11.58
Tm	0.40	0.27	0.50	0.55	0.38	0.20	0.28	0.08	0.23	0.19	2.03	1.90	1.36
Yb	3.01	1.35	5.09	4.54	4.15	2.29	2.30	–	1.68	1.36	14.54	12.47	10.83
Lu	0.40	0.36	0.65	0.91	0.79	0.49	0.50	0.10	0.45	0.40	1.71	1.55	1.63
Hf	0.23	0.06	0	0.12	0.11	0.24	0.07	0.17	0	0.10	4.48	2.72	3.38
Th	0	0.42	0.05	0.17	0	0.10	0	0	0	0	0.33	0.10	0.17
U	0	0.01	0	0.17	0	0.06	0	0.01	0	0	0.03	0.02	0.02
ΣREE	9.20	4.91	12.11	14.69	9.30	5.65	8.13	2.06	4.21	4.03	167.97	152.01	137.31
ΣHREE	6.94	4.19	11.28	11.85	9.25	5.22	6.72	1.77	3.86	3.93	79.58	70.89	64.56
Yb_N/Gd_N	26.2	–	14.98	5.91	1.86	–	7.11	–	26.07	5.60	1.2	1.0	1.1

Table 4. LA-ICP-MS U–Pb isotope data and calculated ages (Ma) for zircons from sample Tur76A. Sub-concordant and discordant data are indicated in italic. Analyses were performed on B-scan mode (c – core; r – rim). All zircons in thin-section are in symplectitic corona.

Spot	$^{207}Pb/^{206}Pb$	±1σ	$^{206}Pb/^{238}U$	±1σ	$^{207}Pb/^{235}U$	±1σ	Rho	$^{207}Pb/^{206}Pb$	±1σ	$^{206}Pb/^{238}U$	±1σ	$^{207}Pb/^{235}U$	±1σ	Concodant ages	2σ	Discordance (%)
Separated zircons																
227-r	0.05629	0.00148	0.07491	0.00131	0.58173	0.01317	0.77520	464	12	466	8	466	11	**466**	**±15**	**0.02**
266-c	0.05522	0.00189	0.07007	0.00125	0.53272	0.01648	0.57470	421	14	437	8	434	13	**436**	**±15**	**0.7**
157-int	0.05202	0.00115	0.04694	0.00082	0.33727	0.00612	0.96500	286	6	296	5	295	5	**295**	**±9**	**0.2**
145-c	0.05757	0.00123	0.08069	0.00139	0.64204	0.01105	0.99000	513	11	500	9	504	9	**513**	**±9**	**–0.7**
181-c	0.05528	0.0011	0.07057	0.00123	0.53921	0.00853	0.99000	424	8	440	8	438	7	**434**	**±6**	**0.4**
157-r	0.05515	0.0011	0.06443	0.00113	0.49085	0.00774	0.99000	418	8	403	7	405	6	**413**	**±6**	**–0.7**
181-r	0.0524	0.0011	0.04742	0.00083	0.34343	0.00583	0.99000	303	6	299	5	300	5	**303**	**±7**	**–0.4**
204-c	0.05242	0.00128	0.04418	0.00078	0.31845	0.00654	0.85690	304	7	279	5	281	6	**279**	**±9**	**–0.7**
204-r2	*0.05337*	*0.00154*	*0.0448*	*0.00081*	*0.32965*	*0.00843*	*0.70920*	*345*	*10*	*283*	*5*	*289*	*7*	*283*	*±10*	*–2.4*
145-r	*0.05613*	*0.00109*	*0.08593*	*0.00147*	*0.66627*	*0.00981*	*0.99000*	*458*	*9*	*531*	*9*	*518*	*8*	–		*2.4*
204-r	*0.0668*	*0.0013*	*0.06379*	*0.00111*	*0.58889*	*0.00878*	*0.99000*	*832*	*16*	*399*	*7*	*470*	*7*	–		*–17.9*
215-c	*0.0793*	*0.00166*	*0.04874*	*0.00089*	*0.53321*	*0.00915*	*0.99000*	*1180*	*25*	*307*	*6*	*434*	*7*	–		*–41.4*
227-c	*0.0612*	*0.00129*	*0.05626*	*0.00099*	*0.47556*	*0.00807*	*0.99000*	*646*	*14*	*353*	*6*	*395*	*7*	–		*–12*
227-int	*0.06155*	*0.00129*	*0.07699*	*0.00134*	*0.65448*	*0.01096*	*0.99000*	*659*	*14*	*478*	*8*	*511*	*9*	–		*–6.9*
Zircons in thin-section																
3-c	0.05397	0.00563	0.05517	0.00125	0.40907	0.04166	0.98400	370	39	346	8	348	35	**345**	**±4**	**–0.6**
12-r	0.05245	0.003	0.04735	0.00079	0.33768	0.01867	0.26400	305	17	298	5	295	16	**298**	**±10**	**0.9**
9-c	0.0516	0.00526	0.04597	0.00190	0.32831	0.03253	0.99000	268	27	290	12	288	29	**291**	**±6**	**0.5**
4-r	0.05438	0.00715	0.04527	0.00140	0.32748	0.04195	0.30300	387	51	285	9	288	37	**285**	**±17**	**–0.8**
11-c	0.05156	0.00264	0.04405	0.00057	0.31288	0.01539	0.65500	266	14	278	4	276	14	**278**	**±6**	**0.5**
12-c	*0.05345*	*0.00224*	*0.04375*	*0.00053*	*0.32263*	*0.01291*	*0.45200*	*348*	*15*	*276*	*3*	*284*	*11*	*276*	*±6*	*–2.9*

Table 5. Trace-element composition (in ppm) in selected zircon domains from sample Tur76A.

	03-zrn266c	07-zrn227r	10-zrn181c	11-zrn157r	13-zrn145c	09-zrn181r	zrn181Ar	zrn181Cr	12-zrn157int	14-zrn12c	15-zrn11c	04-zrn215c	05zrn215r	06zrn227c
Sc	215	224	211	192	260	189	161	162	197	229	217	208	207	212.55
Ti	13	22	7.26	16.33	12.44	9.19	4.98	6.92	10.52	13.33	25	8.59	12.71	85
Sr	1.12	0.23	0.76	1.24	0.52	0.27	0.15	0	0.37	0.56	0.48	0.15	0.08	0.29
Y	840	1290	2696	3652	2124	242	191	241	916	401	453	443	334	1238
Nb	3.23	3.90	11	20.56	7.86	3.77	11.08	10.76	5.92	4.43	3.58	3.68	3.99	4.07
Ba	0.17	–	1.91	1.24	0.56	–	0	0	0.47	–	0.36	–	–	0.42
La	0.22	0.04	0.37	2.76	–	0.03	0.05	0	0.09	–	–	–	–	0.06
Ce	7.86	12.72	15.78	41.63	21.35	2.27	1.85	2.29	4.25	3.71	4.16	4.87	4.74	8.12
Pr	0.04	0.07	0.13	0.91	0.10	0.02	0	0	0.03	0.03	–	0.10	0.01	0.06
Nd	0.77	1.02	2.37	6.15	0.77	0.10	0	0.24	0.95	–	–	0.52	0.30	1.17
Sm	2.40	2.75	4.99	8.70	4.54	0.43	0.75	0	1.72	–	0.66	1.48	0.51	2.87
Eu	0.43	0.31	0.81	1.05	0.61	0.35	0.18	0.31	0.41	0.59	0.70	0.32	0.33	0.47
Gd	11.75	16.64	44.18	70.18	27.33	2.65	2.03	2.52	11.20	5.66	7.44	7.57	5.08	20.81
Tb	5.07	6.79	17.12	25.84	10.59	1.18	0.69	1.19	4.91	2.28	2.81	2.80	1.96	7.60
Dy	64.09	94.31	237.74	337.01	147.38	17.09	11.71	16.57	68.96	30.16	42.48	35.97	22.17	99.05
Ho	26.33	40.37	94.74	132.08	69.72	7.41	4.83	6.29	30.59	12.77	15.12	13.40	10.28	39.12
Er	134.81	198.21	430.11	566.29	329.45	38.57	26.43	34.96	157.16	64.61	72.22	61.75	48.19	193.2
Tm	31.05	46.43	93.40	115.80	76.50	9.39	6.23	7.67	35.75	13.09	14.44	13.18	11.20	41.92
Yb	309.52	459.61	895.92	1021	793.06	103.16	73.26	85.77	375.36	166.50	169.13	128.94	114.92	414.46
Lu	61.69	94.34	172.64	186.28	159.71	24.21	17.65	20.02	79.47	36.05	32.62	26.55	22.16	82.29
Hf	11878	14145	14729	12329	15554	12680	10114	9664	12517	14682	13260	10600	10785	12653
Ta	0.39	0.82	3.94	5.13	1.31	0.65	0.28	0.35	1.29	2.08	0.77	0.65	0.66	0.73
Pb	6.69	6.59	7.26	10.28	16.99	4.06	2.04	2.60	8.04	4.25	3.81	3.38	1.52	3.39
Th	59.10	192.30	180.75	250.12	344.07	48.53	36.02	53.68	89.75	175.72	170.05	111.80	55.73	105.8
U	191.16	519.56	752.87	621.68	817.36	531.46	384.82	482.10	851.09	1670.60	419.76	276.35	155.66	238.12
Th/U	0.31	0.37	0.24	0.40	0.42	0.09	0.09	0.11	0.10	0.10	0.40	0.40	0.36	0.44
Eu/Eu*	0.25	0.14	0.17	0.13	0.17	1.0	0.45	–	0.29	–	0.97	0.30	0.62	0.19
ΣHREE	644	957	1986	2454	1614	204	143	175	763	331	356	290	236	898
ΣREE	656	974	2010	2516	1641	207	146	178	771	335	362	297	242	911
Yb_N/Gd_N	32.56	34.14	25.06	17.96	35.87	48.12	44.61	42.08	41.42	36.36	28.10	21.05	27.96	24.62
Age (Ma)	436	466	434	413	513	303	303	303	295	298	278	–	–	–

Table 6. Mean major element analyses of amphiboles in the different textural sites from sample Tur76A.

	In matrix ($n = 13$)		In garnet ($n = 4$)		In corona of garnet ($n = 16$)		In corona of clinopyroxene ($n = 7$)	
	X	σ	X	σ	X	σ	X	σ
SiO_2	40.26	0.26	39.71	0.30	40.76	0.75	40.64	0.62
TiO_2	2.71	0.18	2.80	0.34	2.44	0.26	2.66	0.30
Al_2O_3	12.35	0.24	12.43	0.14	12.83	0.62	12.25	0.21
FeO	15.44	0.50	15.18	0.36	14.00	0.80	15.24	0.38
MnO	0.05	0.06	0.05	0.04	0.04	0.06	0.06	0.05
MgO	9.71	0.17	9.75	0.04	10.45	0.29	9.70	0.16
Na_2O	2.24	0.12	2.28	0.07	2.22	0.11	2.13	0.06
K_2O	2.07	0.09	2.08	0.13	2.06	0.11	2.01	0.06
CaO	11.91	0.19	11.92	0.12	12.01	0.21	11.82	0.26
Total	96.73	0.51	96.20	0.23	96.81	0.48	96.52	0.39
Number of oxygens: 23								
Si	6.17	0.02	6.12	0.04	6.19	0.07	6.22	0.07
Al	2.23	0.04	2.26	0.03	2.29	0.09	2.21	0.04
Fe^{2+}	1.98	0.06	1.96	0.05	1.78	0.11	1.95	0.05
Mg	2.22	0.04	2.24	0.01	2.37	0.07	2.22	0.04
Na	0.66	0.04	0.68	0.02	0.65	0.03	0.63	0.02
K	0.40	0.02	0.41	0.03	0.40	0.02	0.39	0.01
Ca	1.96	0.02	1.97	0.02	1.95	0.05	1.94	0.04
Ti	0.31	0.02	0.32	0.04	0.28	0.03	0.31	0.03
Mn	0.01	0.01	0.01	0.00	0.01	0.01	0.01	0.01
Mg number	52.84	1.15	53.38	0.54	57.12	1.71	53.17	0.38

to Kretz, 1983) shows lower contents of Sc (75 ppm), V (546 ppm) and Cr (135 ppm) and higher contents of Ti (17057 ppm) and Ni (150 ppm) than those of the matrix (Sc = 143 ppm; V = 824 ppm; Cr = 374 ppm; Ti = 14448 ppm; Ni = 132 ppm); another crystal (amph 3 in Fig. 9) included in the peripheral part of garnet shows Sc, V, Cr, Ti and Ni contents similar to those of the matrix.

Regarding REE distribution, the amphibole occurring in corona around garnet defines two distinct populations having similar convex patterns at different levels of REE abundances (Table 7; Fig. 10): type 1 (Fig. 2a, bottom right; Fig. 4a) occurs near the REE-poor bights of garnet rim and shows high REE contents (680 ppm) and Yb_N/Gd_N ratio (0.71); type 2 (Fig. 2a, bottom right) occurs near the REE-rich lobes of garnet rim (Fig. 4a) and has lower REE contents (493 ppm) and Yb_N/Gd_N ratio (0.50). Amphibole in matrix shows lower REE contents (441 ppm) and nearly flat HREE pattern ($Yb_N/Gd_N = 1.12$). Amphibole occurs around the nodule of clinopyroxenite, proving a pattern which is intermediate between amphibole type 1 and amphibole in matrix, whereas its Cr and Ti contents are similar to those of amphibole type 2 (Fig. 9). The two crystals included in garnet (amph 1 and amph 3, Fig. 10) display lower HREE contents (127 ppm) and a more fractionated pattern ($Yb_N/Gd_N = 0.20$) than all the other amphiboles.

To summarize, on the basis of trace-element distribution (Cr, Ni, Ti, Sc, V and REE) and of textural features, it appears that different types of amphibole occur in the studied sample (Figs 9, 10): (1) Amphiboles in matrix and in corona near bights of garnet (type 1 REE-rich) show quite similar flat REE patterns and similar contents of Ti and Cr. (2) Drop-like amphibole included in garnet core displays fractionated REE pattern, high Ti and low Cr contents. According to Acquafredda *et al*. (2008), the drop-like inclusions of plagioclase, amphibole and clinopyroxene in porphyroblastic garnet represent relict phases recording the pre-granulite stage. (3) Amphibole in corona near garnet lobes (type 2 REE-poor) shows fractionated REE pattern, high Cr contents and low Ti contents. (4) Amphibole from corona of clinopyroxenite nodule shows similarities with amphibole of type 1 (similar REE pattern), amphibole of type 2 (high Cr contents) and amphibole from matrix (similar Ti contents).

Biotite is present only in corona around garnet. It is Mg rich (Mg number 64 on average) and shows very low REE contents.

5.b. Comparison with intermediate granulite GRT3

The chemical compositions of minerals in sample GRT3 (Fornelli *et al.* 2014) are summarized here. The porphyroblastic garnet (Fig. 2b) is an almandine (48–59 mol %) with grossular around 16 mol % and Mg number decreasing from core (41) to peripheral domains (27). The REEs and Zr (averaging 146 ppm) concentrations are very high, particularly along the core-rim profile; the ΣHREE, on average, gradually decreases from 2463 ppm to 1434 ppm and increases towards the lobes up to 5874 ppm (rim 2A, lobe in Fig. 4b). Millimetric bights interrupt the continuity of the former rim and expose the interiors of garnet (Fig. 4b) approaching their REE contents (site 'c' in Fig. 4b). This distribution of the HREE allowed three regions of garnet to be distinguished (Fig. 4b): (1) an inner core region (average ΣHREE = 2463 ppm); (2) an outer core (average ΣHREE = 1434 ppm); and (3)

https://doi.org/10.1017/S001675681700067X Published online by Cambridge University Press

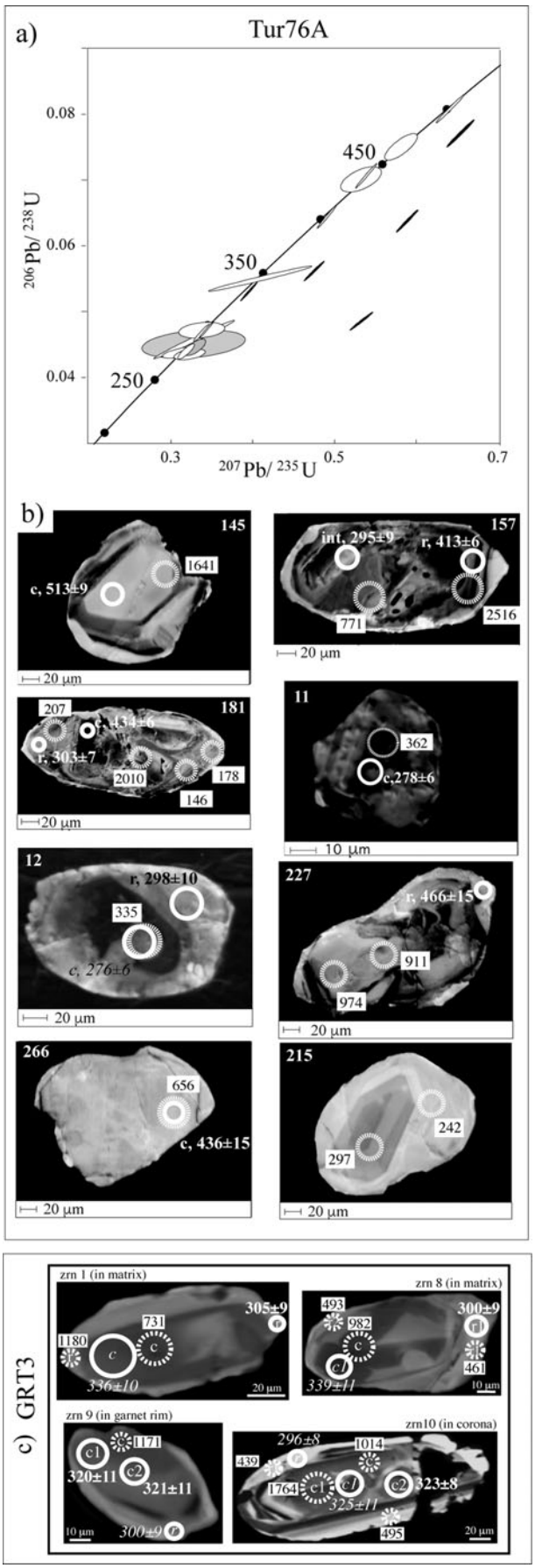

Figure 7. (a) Concordia diagram with concordant (white ellipse), sub-concordant (grey ellipse) and discordant (black ellipse) U–Pb data in sample Tur76A. (b) VPSED images of the analysed zircons in sample Tur76A. Circles indicate the U–Pb spot ages. The concordant ages are given with normal characters, whereas the ages with low probability of concordance are shown in italics. Dotted circles indicate the trace-element spot analyses. The numbers in white boxes indicate ΣREE. On rim of zircon 181 three spot analyses were performed. (c) VPSED images of zircons in sample GRT3, modified from Fornelli *et al.* (2014).

a peripheral region, about 3 mm thick, in which the ΣHREE increases at the lobes (rim 2A in Fig. 4b) and decreases at the bights (rim 1A and site 'c' in Fig. 4b). The chondrite-normalized patterns of REE relative to the core, outer core and rim regions (rim 1A, rim 2A and site 'c' in Fig. 4b) are given in Figure 5b and are derived from Fornelli *et al.* (2014). The distribution of HREE at the margin of garnet in GRT3 is similar to that of garnet in sample Tur76A: HREE-poor bights and HREE-rich lobes. Fornelli *et al.* (2014) interpreted the high abundances of HREE at the lobes as due to consumption of garnet and redistribution of HREE via intra-crystalline diffusion in smaller volumes of the crystal ('held back effect' according to Harley & Kelly, 2007).

Garnet of the amphibole-bearing sample Tur76A has comparable end-member profiles, but REE abundances are distinctly lower than those of garnet in the sample GRT3 (without amphibole) even if the REE budget in the two reservoirs was similar (Table 1, Fig. 3). The present rim with lobes and bights shows the same HREE behaviour as in GRT3.

In sample GRT3 orthopyroxene is present in matrix and in symplectitic corona around garnet with homogeneous composition (Enstatite 64–68; Mg number 65–68) and REE slightly fractionated patterns (Yb_N/Gd_N ratio from 9 to 13, Fig. 6c). From Figure 6c, however, it appears that the average of REE in some crystals from symplectitic corona near the lobes of garnet (rim 2A) is lower (6.41 ppm) and less fractionated (Yb_N/Gd_N = 2.85) than the REE average in orthopyroxene from matrix (13–20 ppm) and in the residual corona (9–10 ppm). Orthopyroxene in corona around garnet from sample Tur76A shows REE contents ranging from 4.91 ppm to 14.69 ppm (Table 3), slightly higher than those of orthopyroxene from matrix (2.06–4.21 ppm). The variability of REE abundance in orthopyroxene from corona of garnet is unrelated to bights or lobes of garnet; the orthopyroxene compositon in corona of garnet has therefore been averaged (see Section 6.b below).

In the sample GRT3, concordant and sub-concordant ages of zircons range from 289 ± 9 Ma to 357 ± 11 Ma (Fornelli *et al.* 2014). The REE data of ten micro-domains on four dated zircon crystals are given in Figure 7c (from Fornelli *et al.* 2014). The analysed domains have moderate to high Th/U ratios (0.15–0.57), which mainly tend to decrease from core to rim. The high Th/U ratio in the core could suggest a magmatic origin of zircons; the lower Th/U ratio in

https://doi.org/10.1017/S001675681700067X Published online by Cambridge University Press

Table 7. Means of trace elements (in ppm) in amphiboles from the different textural sites of the sample Tur76A.

	In matrix		In garnet (amph 1)			In corona of garnet (REE-rich type 1)		In corona of garnet (REE-poor type 2)		In corona of clinopyroxene	
	X ($n = 9$)	σ	X ($n = 2$)	σ	In garnet (amph 3)	X ($n = 9$)	σ	X ($n = 6$)	σ	X ($n = 2$)	σ
Y	255	33.56	154	0.21	217	453	37.69	290	57.97	326	6.31
Zr	–	–	–	–	–	60	35.36	18	28.93	–	–
Ti	14448	631.07	17057	374.41	14260	13610	717.37	12344	710.87	14072	608.71
Cr	374	111.51	135	8.24	664	409	107.06	685	47.37	688	23.98
V	824	110.76	546	4.81	843	934	94.12	1000	92.35	999	6.09
Ni	132	10.14	150	0.41	128	144	7.61	123	10.94	131	6.84
Zn	162	17.11	196	4.26	229	207	24.62	216	18.79	206	4.86
Sc	143	14.85	75	0.54	109	182	58.27	198	56.83	183	2.24
Sr	61	6.60	60	3.65	57	69	13.35	64	9.15	53	14.06
Nb	20	1.18	16	0.85	19	19	0.90	19	1.43	16	2.08
Ba	382	27.52	491	3.36	393	433	50.03	399	25.29	332	65.12
La	32.43	1.24	32.43	0.73	32.83	35.86	3.17	30.31	2.03	29.63	0.99
Ce	113.36	5.52	121.99	3.33	126.17	142.74	11.76	119.10	5.82	117.9	0.04
Pr	18.38	1.84	21.79	0.22	20.33	25.50	2.85	20.61	1.36	20.22	0.42
Nd	91.40	13.66	116.49	1.77	107.02	142.99	19.64	103.79	10.54	109.44	0.76
Sm	26.78	5.16	34.32	5.82	27.98	47.14	7.64	32.73	5.41	35.41	0.63
Eu	4.88	0.68	7.67	0.29	5.61	6.73	0.62	5.44	0.38	4.97	0.02
Gd	30.05	6.04	43.99	1.54	47.06	62.34	9.25	45.14	4.34	44.83	1.92
Tb	6.21	1.11	7.41	0.13	7.70	12.90	1.72	8.87	0.80	8.78	0.15
Dy	45.07	6.79	44.15	0.25	48.99	89.86	9.96	60.50	9.16	60.81	1.10
Ho	10.20	1.11	7.02	0.32	9.27	19.62	1.89	12.70	1.74	13.70	0.41
Er	28.13	3.76	13.99	0.13	19.34	49.35	4.42	30.27	6.86	36.98	0.46
Tm	3.98	0.39	1.55	0.30	2.46	5.91	0.59	3.26	0.96	4.84	0.15
Yb	26.70	2.73	7.59	0.92	13.18	35.33	3.99	17.97	6.26	31.83	0.17
Lu	3.50	0.31	0.90	0.02	1.23	4.23	0.70	1.85	0.68	4.04	0.12
Hf	3.57	0.60	4.99	0.11	2.15	4.54	1.17	3.82	0.65	3.99	0.68
Th	0.67	0.13	0.73	0.09	0.69	0.67	0.13	0.69	0.18	0.53	0.06
U	0.15	0.02	0.17	0.02	0.09	0.17	0.07	0.17	0.06	0.11	0.04
ΣREE	441.07	44.79	461	11.71	469	680.49	61.61	492.54	24.77	523.36	2.89
ΣHREE	153.85	20.82	126.6	0.57	149.23	279.54	25.15	180.55	24.64	205.79	0.01
Yb_N/Gd_N	1.12	0.14	0.21	0.03	0.35	0.71	0.10	0.50	0.20	0.87	0.03

The analyses were performed by LA-ICP-MS (minimum detection limits at 99 % confidence level were $<10^{-5}$ for most of the elements; precision and accuracy were assessed on the BCR-2 USGS reference glass and are more than 6 % relative).

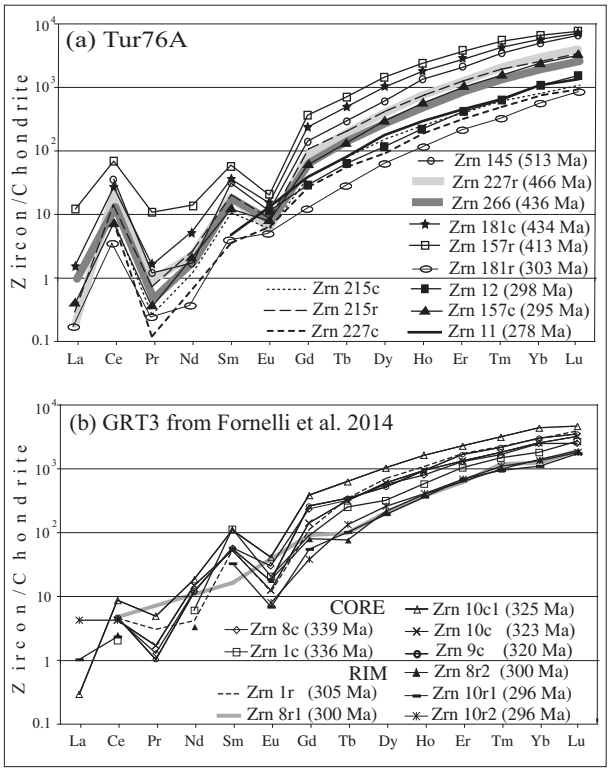

Figure 8. (a) REE patterns of analysed zircons in sample Tur76A normalized to chondrite (McDonough & Sun, 1995). REE pattern of zircon rim 181 is the average of three spot analyses. Zrn 215 and zrn 227 in sample Tur76A are undated. (b) REE patterns of zircons in sample GRT3, from Fornelli *et al.* (2014).

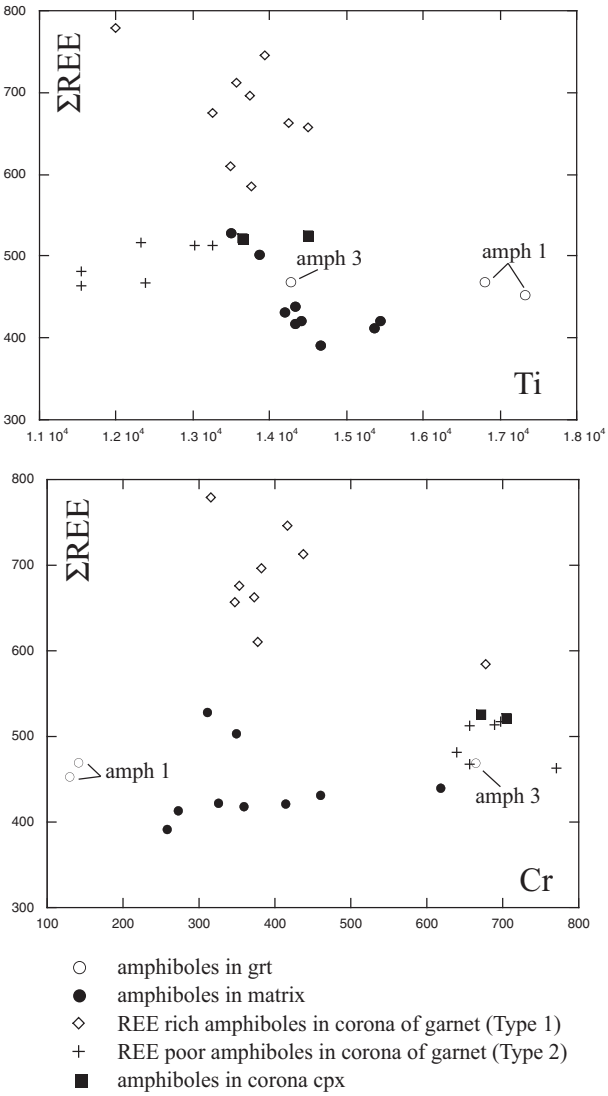

Figure 9. ΣREE v. Ti and Cr in amphiboles from the sample Tur76A. Two analyses were performed on amph 1 included in garnet (see Figs 2–4).

the rims indicates a new growth assisted by aqueous fluids or hydrous melts (Zhou *et al.* 2011; Fornelli *et al.* 2014).

The ΣREE in the zircon domains older than 305 Ma has high values (731–1763 ppm), whereas in the zircon domains dated at 305–296 Ma, ΣREE varies from 1180 to 439 ppm and defines steep patterns (Fig. 8b) with Yb_N/Gd_N ratios in the range 14–35. On the whole, it appears that the REE content of zircon in the amphibole-free sample (GRT3) is higher than in the amphibole-bearing sample (Tur76A), as occurs for garnet.

6. Discussion

The studied sample (amphibole-bearing Tur76A) has mafic composition and contains garnet with about 16 mol % of grossular and zircons showing core-rim structures. These characteristics are also shown by the biotite-bearing sample GRT3, which has an intermediate composition (Fornelli *et al.* 2014). The main difference between the two samples is that of higher REE contents in garnet, zircon and orthopyroxene in the sample GRT3. Both rocks derive from the same crust level, and they were equilibrated under similar thermobarometric conditions (Fig. 1c): *P* from 1.0 GPa to 0.7 GPa; *T* from 900° to 700 °C; geothermal gradient from 21 °C km^{-1} to 29 °C km^{-1} in a timespan between 350 Ma and 280 Ma (Fornelli *et al.* 2011; Fornelli, Pascazio & Piccarreta, 2011; Fornelli *et al.* 2012).

In both samples the reabsorbed garnet is surrounded by continuous symplectitic corona which formed during the decompression, consisting of plagioclase + orthopyroxene + biotite ± amphibole (Fig. 2). The present rim of garnets shows REE-rich lobes and deep millimetre-scale REE-depleted bights, reflecting the metamorphic history and *P-T* conditions during the decompression phases. In the initial step of garnet dissolution, under low geothermal gradient (21 °C km^{-1}), intra-crystalline diffusion favoured a higher concentration of REE in the lobes of garnet. Subsequently, under increasing geothermal gradient (29 °C km^{-1}), a faster dissolution of garnet caused chemical material transfer towards the reaction products, forming REE-depleted bights of garnet.

The presence of amphibole in the symplectitic corona in the sample Tur76A affects the REE contents in coexisting zircon, garnet and orthopyroxene

https://doi.org/10.1017/S001675681700067X Published online by Cambridge University Press

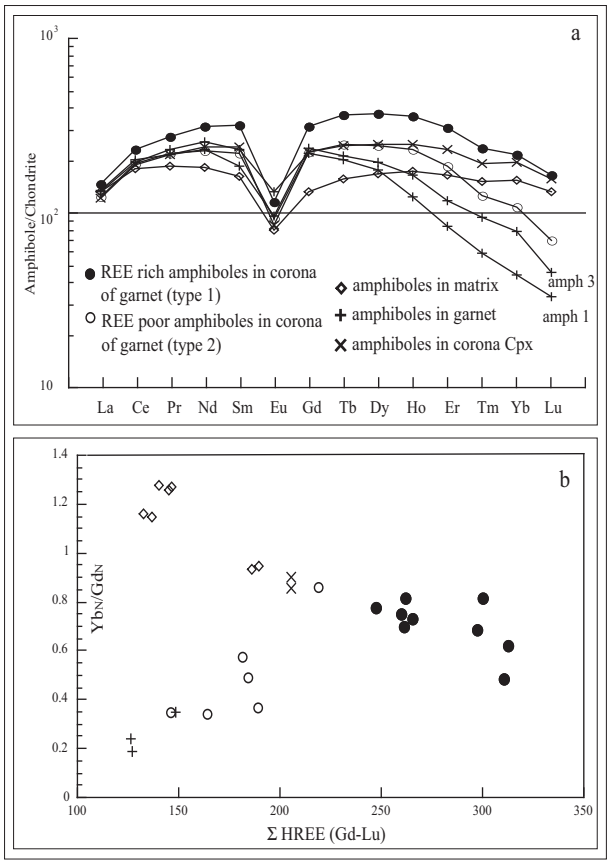

Figure 10. (a) Averaged REE patterns and (b) Yb_N/Gd_N ratio v. HREE of amphiboles from sample Tur76A.

because it is an effective competitor for middle and heavy REEs. The present data allow the REE distribution coefficients for the pairs zircon–garnet, orthopyroxene–garnet and amphibole–garnet to be calculated, and the values of approached equilibrium during the metamorphic evolution of mafic and intermediate granulites to be hypothesized. Zircon–garnet and orthopyroxene–garnet pairs are compared with data from the literature, allowing information to be gained about the equilibrium conditions for amphibole–garnet pairs.

6.a. Zircon–garnet relationships

Several empirical determinations and experimental studies of DREE (zircon–garnet) have been performed mainly on metapelitic and granitic systems. The results interpreted as indicating chemical equilibrium are notably different: (1) REE nearly equally partitioned between zircon and garnet (D *c.* 1; Whitehouse & Platt, 2003; Harley & Kelly, 2007; Taylor *et al.* 2015); (2) DREE fractionated patterns assuming high DREE values (> 4 from Er to Lu) at decreasing *T* (Rubatto & Hermann, 2007); and (3) DREE more fractionated from Gd to Lu, but with lower values ranging from 0.18 (D_{Gd}) to 3.12 (D_{Lu}) in an intermediate granulite (Fornelli *et al.* 2014). In this paper, DREE zircon/garnet in a mafic granulite have been calculated to gain more information.

In the studied sample (Tur76A), the pre-Silurian zircon domains have not been considered to evaluate the zircon–garnet relationships because the garnet was missing during that time, as shown by its oldest Sm/Nd age at 354 Ma in a sample taken in the same area (Duchene *et al.* 2013).

When normalized to garnet core, the zircon domain, dated 303 Ma (zrc 181; ΣHREE = 177 ppm obtained by averaging three spot analyses), overlaps the previously sets; this is interpreted as suggestive of equilibrium of zircon domains dated at 339–336 Ma, 325–320 Ma and 305 Ma combined with the outer core of garnet in the sample GRT3 (Table 8; Fig. 11a; Fornelli *et al.* 2014). The overlap of the partition coefficients is evident, notwithstanding the different REE contents in both garnet and zircon in the two samples (Fig. 11a). Around 300 Ma ago the original garnet rim experienced dissolution up to 279 Ma (Fornelli *et al.* 2011), forming the present rim with HREE-rich lobes and HREE-poor bights (Figs 2, 4). The zircon domains in symplectitic corona (zrc 12, zrc 11) around garnet seem to have formed together with amphibole of symplectitic corona when the original garnet rim underwent dissolution, as shown by ages of 298 Ma and 278 Ma which are consistent with the timing of garnet dissolution. The $DHREE_{zrn/grt}$ values have therefore been calculated for the combination of zircon dated 298 Ma with the near REE-rich garnet lobe, which produced DREE patterns far from equilibrium. The values are in fact too low, similarly to that for the zircon domain dated 300 Ma in a comparable site of sample GRT3 (Fig. 11b). Subsequent incremental garnet dissolution produces HREE-poorer bights around 279 Ma (Fornelli *et al.* 2011) and the formation of new zircon with low HREE contents (zrc 11 dated at 278 Ma with ΣHREE 356 ppm). The low HREE content of zircon was probably conditioned by simultaneous crystallization of REE-rich amphibole in symplectitic corona. The zircon domain dated 278 Ma together with the undated zircon having low HREE contents (zrc 215) were combined with HREE-poor garnet bights; $DHREE_{zrn/grt}$ values show a positive trend (Fig. 11c) with increasing values from Gd to Lu which, however, are slightly different from those hypothesized as equilibrium values in current literature (Whitehouse & Platt, 2003; Rubatto & Hermann, 2007; Fornelli *et al.* 2014). These calculated values (Table 8, Fig. 11c) tend to be higher than the set indicated by Fornelli *et al.* (2014), mirroring the trend of Rubatto & Hermann (2007) towards temperature around 800 °C (Rubatto & Hermann, 2007). In the studied case, an increase of the geothermal gradient from 21 °C km^{-1} to 29 °C km^{-1} (Fornelli, Pascazio & Piccarreta, 2011) is actually consistent with temperature around 800 °C. These trends (Fig. 11c) probably reflect approached equilibrium between the considered zircon–garnet domains at 278 Ma in mafic granulite.

https://doi.org/10.1017/S001675681700067X Published online by Cambridge University Press

Table 8. Empirical HREE distribution coefficients approaching equilibrium calculated between zircons having different ages and various regions of garnet (core, garnet bight near zircon 11, REE-poor garnet bights) in sample Tur76A. The composition of zircon 181 rim was obtained averaging three spot analyses. The mean of $DHREE_{zrn/grt}$ is also reported, interpreted as equilibrium, from Fornelli *et al*. (2014). Zircon 215 is undated.

		Tur76A			
	GRT3 $DHREE_{zrn/grt}$ mean	Zrn 181 rim (303 Ma) garnet core	Zrn 11 (278 Ma) near garnet bight	Zrn 215 core REE-poor garnet bight	Zrn 215 rim REE-poor garnet bight
Gd	0.18	0.17	0.29	0.56	0.37
Tb	0.22	0.22	0.30	0.66	0.46
Dy	0.32	0.34	0.46	0.87	0.53
Ho	0.53	0.48	0.62	1.14	0.88
Er	0.89	0.75	0.88	1.55	1.21
Tm	1.37	1.03	0.97	1.89	1.61
Yb	1.86	1.40	1.34	2.22	1.97
Lu	3.12	2.06	1.91	2.95	2.46

To summarize, the zircon domain dated at 303 Ma combined with the core of the coexisting garnet (diachronic growth of garnet from 354 Ma to 309 Ma in Duchene *et al.* 2013) probably shows approached equilibrium (Fig. 11a), assuming $DHREE_{zrn/grt}$ values similar to those interpreted by Fornelli *et al.* (2014) as suggestive of equilibrium in the sample GRT3. The zircon domain dated 298 Ma, combined with the lobes of garnet (HREE-rich), produces patterns far from equilibrium as for the zircon dated 300 Ma in the GRT3 sample occurring in a similar site (Fig. 11b). The younger zircon domain in symplectitic corona of garnet (278 Ma in sample Tur76A), normalized to composition of the garnet bights, produces $DHREE_{zrn/grt}$ values suggestive of possible chemical equilibrium (Fig. 11c). From all these observations it emerges that: (1) a diachronic growth of garnet occurred in the considered granulites (339 Ma in sample GRT3; 303 Ma in sample Tur76A); (2) dissolution of garnet began at *c.* 300–298 Ma, forming HREE-rich rim preserved in the lobes under disequilibrium conditions due to intra-crystalline diffusion and sequestration of HREE in the former rim of garnet; and (3) at 278 Ma, REE-poor garnet bights probably formed in equilibrium with nearby zircon due to inter-crystalline diffusion, favoured by the presence of fluids or melts, as shown by biotite and amphibole growth in corona. The crystallization of REE-rich amphibole in garnet corona near bights accounts for the low HREE content in the zircon dated at 278 Ma.

6.b. Orthopyroxene–garnet relationships

In sample Tur76A, orthopyroxene from matrix is slightly lower in REE (2.06–4.21 ppm) in comparison with orthopyroxene from corona (4.91–14.69 ppm ppm); the REE content of the latter is unrelated to lobes or bights of garnet. The mean composition of orthopyroxene in symplectitic corona has been considered in the following calculations. The $DHREE_{opx/grt}$ values calculated between orthopyroxene from matrix and garnet core as well as those of the combinations orthopyroxene from corona and REE-poor garnet rim (bights) overlap many of the empirical equilibrium values suggested by Harley *et al.* (2001) and Harley & Kelly (2007) (Fig. 12, Table 9). Instead, the $DHREE_{opx/grt}$ values calculated for orthopyroxene from corona and REE-rich garnet rim (lobes) produce data mostly outwith the equilibrium range (Fig. 12, Table 9).

The lack of equilibrium of orthopyroxene from corona with REE-rich lobes of garnet rim suggests that the REE 'held back effect' at garnet rim, as also evidenced by $DHREE_{zrn/grt}$, is due to low HREE diffusion during garnet dissolution, which does not promote equilibrium with the corona minerals (Tajcmanova *et al.* 2014). On the other hand, DREE opx-grt patterns falling outwith the equilibrium range were demonstrated by Fornelli *et al.* (2014) in the sample GRT3 combining orthopyroxene in symplectitic corona and REE-rich lobes of garnet rim (Fig. 12).

6.c. Amphibole–garnet relationships

Figure 13 reports the $DREE_{amph/grt}$ patterns of the combinations: (1) included amphibole–garnet core; (2) amphibole from matrix–garnet core; (3) HREE-rich amphibole from corona (type 1) HREE-poor garnet rim (bights); and (4) REE-poor amphibole from corona (type 2) HREE-rich garnet rim (lobes). The calculated values are given in Table 10. It appears that $DREE_{amph/grt}$ trends are clearly different starting from Gd. During the garnet growth, REEs from Gd to Dy prefer amphibole with $D_{Gd\text{-}Dy} \geq 1$ (amphibole in garnet and in matrix with respect to garnet core), whereas REEs from Ho to Lu were sequestrated by garnet. When the garnet was consumed and corona formed under decreasing pressure, initially slow intracrystalline diffusion in garnet caused concentration of REE from Tb to Lu in the new rim (lobes), whereas MREE (Sm-Gd) preferred amphibole (Table 10). Subsequently, fast dissolution of garnet favoured the intercrystalline diffusion, also due to the presence of fluids or melts, and the REEs from Sm to Er preferred the amphibole (DREEs 12.03–1.24), whereas again Tm, Yb and Lu remained in garnet.

https://doi.org/10.1017/S001675681700067X Published online by Cambridge University Press

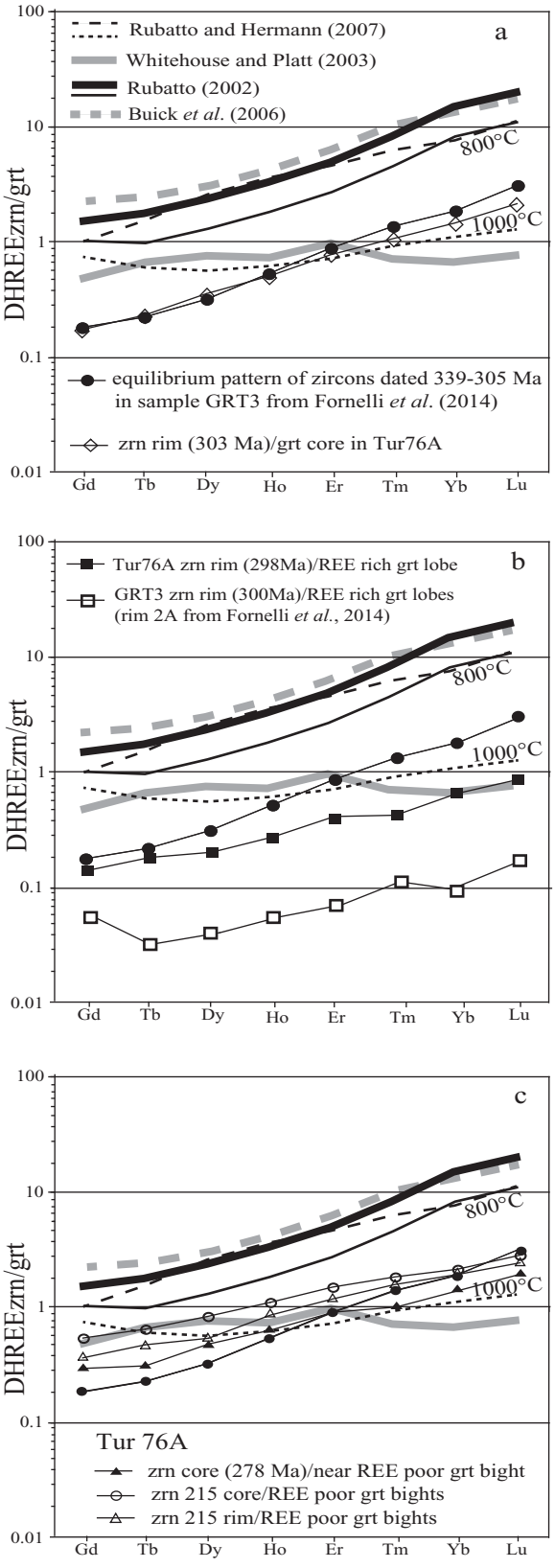

Figure 11. Comparison between calculated $DHREE_{zrn/grt}$ considering zircons in Tur76A sample and those in literature. (a) $DHREE_{zrn(303\ Ma)/grt}$ calculated with respect to garnet core compared with mean of $DHREE_{zrn/grt}$ in sample GRT3 (from Fornelli *et al*. 2014), representing equilibrium conditions. (b) $DHREE_{zrn(298\ Ma)/grt}$ calculated with respect to REE-rich garnet rim (near lobe) showing values far from equilibrium conditions. $DHREE_{zrn(300\ Ma)/grt}$ pattern out of equilibrium in sample GRT3 is reported for comparison. (c) $DHREE_{zrn(278\ Ma)/grt}$ calculated with respect to REE-poor garnet rim (near bight) showing a restored equilibrium in sample Tur76A, are shown and compared with undated zircons (with low HREE contents) normalized to REE-poor bights. $DHREE_{zrn/grt}$ patterns from literature are also reported.

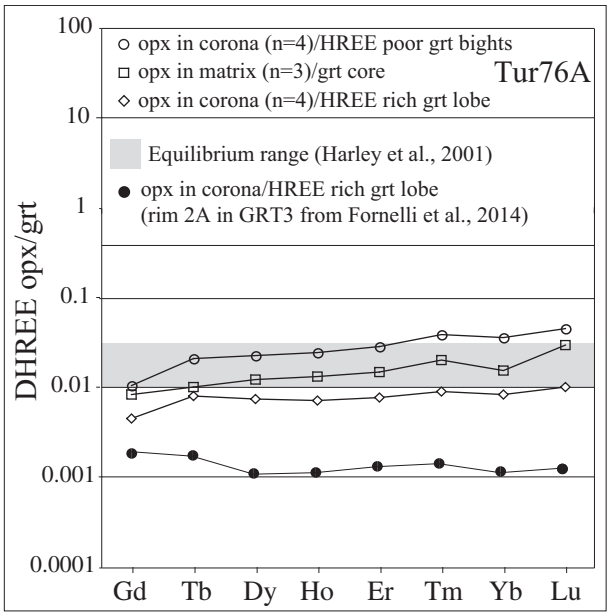

Figure 12. Patterns of the calculated $DHREE_{opx/grt}$ in different textural sites from sample Tur76A compared with $DHREE_{opx/grt}$ of sample GRT3 from Fornelli *et al.* (2014). Grey area represents the equilibrium values suggested by Harley *et al*. (2001).

On the whole, amphiboles give distinct and coherent $DHREE_{amph/grt}$, which follow the metamorphic evolution: (1) during the prograde evolution up to stabilization of orthopyroxene in the matrix (granulite facies), the distribution coefficients show that amphibole prefers MREE (Sm-Dy) and garnet prefers HREE (Ho-Lu) (Fig. 13); (2) during the post-peak decompression under still high temperature the garnet breakdown initiated and intra-crystalline diffusion was effective; REE-poor amphibole (type 2) formed in corona (Fig. 4a); and (3) during subsequent rapid dissolution of garnet (bights), MREE- and HREE-richer (type 1) amphibole formed in corona (Figs 4a, 10).

On the basis of the data obtained from the REE distribution between zircon–garnet and orthopyroxene–garnet, the distribution of REE can be tested between amphibole and garnet reflecting equilibrium or disequilibrium conditions. The amphibole included in garnet probably represents a relict phase (Fornelli *et al.* 2011) and the DHREE pattern indicates chemical disequilibrium; a similar DHREE pattern was displayed by amphibole type 2 (REE-poor) in corona with respect to REE-rich garnet rim (lobes). This fact already emerged from the DHREE values out of equilibrium for zircon and orthopyroxene normalized to REE-rich garnet lobes in the studied samples. Patterns of DREE for amphibole in matrix–garnet core and amphibole

https://doi.org/10.1017/S001675681700067X Published online by Cambridge University Press

Table 9. Empirical REE distribution coefficients calculated between orthopyroxene and garnet in different textural sites in sample Tur76A. Column A provides the $DHREE_{opx/grt}$ data from sample GRT3.

	GRT3	Tur76A		
	A	B	C	D
Gd	0.002	0.009	0.011	0.005
Tb	0.002	0.011	0.022	0.009
Dy	0.001	0.013	0.024	0.008
Ho	0.001	0.014	0.026	0.008
Er	0.001	0.016	0.031	0.008
Tm	0.001	0.022	0.041	0.010
Yb	0.001	0.016	0.038	0.009
Lu	0.001	0.031	0.048	0.011

A: DREE of orthopyroxenes in corona (mean $n = 6$) near HREE-rich garnet lobe normalized to REE-rich garnet rim 2A in GRT3 sample from Fornelli *et al*. (2014). B: sample Tur76A orthopyroxene in matrix ($n = 3$) normalized to garnet core; C: orthopyroxene in corona (n = 4) normalized to HREE-poor garnet bights. D: orthopyroxene in corona (n = 4) normalized to HREE-rich garnet lobe.

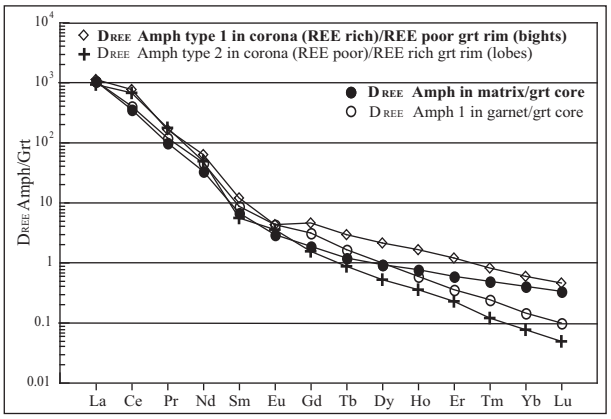

Figure 13. Patterns of the calculated $DREE_{amph/grt}$ in different textural sites and various domains of porphyroblastic garnet in the sample Tur76A are reported. The values interpreted as being indicative of chemical equilibrium are indicated in bold (see legend).

type 1 (REE-rich) of corona – REE-poor garnet bights – display similar trends interpreted as representative of approaching equilibrium conditions. The possible equilibrium conditions between amphibole and garnet are demonstrated by the range of DHREE values shown in Table 10 (highlighted in bold) and mostly by the trend of DHREE tending to rise towards Lu (Fig. 13).

7. Conclusions

The present paper can help to: (1) evaluate the role of amphibole in the control of HREE abundances in competitors such as garnet, zircon and orthopyroxene; (2) define the REE partition among garnet, zircon, orthopyroxene and amphibole in the considered chemical systems monitoring the timing through U–Pb zircon ages; (3) explain the different distribution of REE along the present rim of reabsorbed garnets showing lobes and bights; (4) give further information

Table 10. Empirical REE distribution coefficients calculated between amphiboles in different textural sites and various regions of garnet (core, HREE-poor bights and HREE-rich lobes) in sample Tur76A. The equilibrium values are highlighted in bold.

	A	B	C	D
La	1097	1093	1172	965
Ce	400	362	763	669
Pr	120	99	167	182
Nd	45	34	64	50
Sm	8.95	6.80	12.03	5.58
Eu	4.37	2.92	4.49	3.67
Gd	3.13	**1.88**	**4.58**	1.61
Tb	1.64	**1.24**	**3.03**	0.90
Dy	1.03	**0.94**	**2.17**	0.54
Ho	0.61	**0.76**	**1.67**	0.35
Er	0.35	**0.60**	**1.24**	0.23
Tm	0.25	**0.51**	**0.85**	0.12
Yb	0.15	**0.41**	**0.61**	0.08
Lu	0.10	**0.34**	**0.47**	0.05

A: mean of amph 1 and amph 3 included in garnet normalized to garnet core; B: amphibole in matrix normalized to garnet core; C: REE-rich amphiboles in corona (type 1) normalized to REE-poor garnet bights; D: REE-poor amphiboles in corona (type 2) normalized to REE-rich garnet lobes.

about the chemical equilibrium of zircon–garnet and orthopyroxene–garnet; and (5) explore the possibility of defining equilibrium amphibole–garnet under granulite-facies conditions.

(1) Under granulite-facies conditions, amphibole sequestrates abundant MREE and HREE (Skublov & Drugova, 2003; Storkey *et al.* 2005; Buick *et al.* 2006) causing depletion of REE contents in coexisting competitors (garnet, zircon and orthopyroxene), evident from the comparison of mineral compositions from amphibole-free granulites with amphibole-bearing granulites having a similar budget of REEs.

(2) During decompression, the porphyroblastic garnet underwent dissolution as evidenced by symplectitic corona formed by plagioclase, orthopyroxene, biotite and amphibole. The REE distribution along the reabsorbed garnet rim seems to reflect both the intracrystalline diffusion with slow dissolution rate, resulting in REE-rich domains recorded by lobes, and the inter-crystalline diffusion with fast dissolution, probably assisted by fluids, producing the REE-poor bights.

(3) Steep patterns of $DHREE_{zrn/grt}$ are suggestive of approached equilibrium for zircons dated at 339–320 Ma (Fornelli *et al.* 2014) up to 303 Ma with core or outer core garnet. Subsequently, when consumption of the original rim of garnet started (at *c.* 300–298 Ma), conditions far from equilibrium existed and REE-rich lobes of garnet formed. During the final stage of decompression under an increasing geothermal gradient, a new equilibrium was restored between zircon dated 278 Ma and REE-poor bights of garnet.

(4) $DHREE_{opx/grt}$ values show a wide variation, assuming that values are indicative of equilibrium for some elements when orthopyroxene from matrix and garnet core were considered or orthopyroxene from corona was normalized to REE-depleted garnet bights. The calculated $DHREE_{opx/grt}$ values for the combinations of orthopyroxene in corona and REE-rich garnet lobes are far from equilibrium.

https://doi.org/10.1017/S001675681700067X Published online by Cambridge University Press

(5) Different REE patterns of amphibole are present in the amphibole-bearing sample: (a) amphibole included in garnet and that in corona near the lobes of garnet shows strong depletion from Dy to Lu; and (b) amphibole from matrix and that of corona near bights of garnet displays quite flat HREE patterns with a slight enrichment in MREE. A chemical disequilibrium was inferred between lobes of garnet–zircon and –orthopyroxene from corona, so it is possible that even HREE-poor amphibole of corona was not equilibrated with lobes of garnet. On this basis, the $DHREE_{amph/grt}$ values obtained between amphibole of matrix–garnet core and amphibole from corona near the bights of garnet and REE-poor garnet rim (composition of bights) are assumed to be indicative of equilibrium conditions (DREEs in bold in Table 10). Generally, these values are >1 from Gd to Er (4.58–1.24) and <1 from Tm to Lu (0.85–0.34), even if $D_{amph/grt}$ of Dy, Ho and Er can have values within the range 0.60–0.94.

Acknowledgements. We are grateful to P. Acquafredda for assistance with SEM facilities. We thank two anonymous referees for their valuable suggestions improving the manuscript. The editor Chad Deering is thanked for editorial assistance. The research was financially supported by MIUR and 'Aldo Moro' University of Bari (Italy).

Supplementary material

To view supplementary material for this article, please visit https://doi.org/10.1017/S001675681700067X.

References

Acquafredda, P., Fornelli, A., Paglionico, A. & Piccarreta, G. 2006. Petrological evidence for crustal thickening and extension in the Serre granulite terrane (Calabria, southern Italy). *Geological Magazine* **143**, 1–19.

Acquafredda, P., Fornelli, A., Piccarreta, G. & Pascazio, A. 2008. Multistage dehydration–decompression in the metagabbros from the lower crustal rocks of the Serre (southern Calabria, Italy). *Geological Magazine* **145**, 397–411.

Amodio Morelli, L., Bonardi, G., Colonna, V., Dietrich, D., Giunta, G., Ippolito, F., Liguori, V., Lorenzoni, S., Paglionico, A., Perrone, V., Piccarreta, G., Russo, M., Scandone, P., Zanettin Lorenzoni, E. & Zuppetta, A. 1976. L'arco Calabro-Peloritano nell'orogene Appenninico-Maghrebide. *Memorie Società Geologica Italiana* **17**, 1–60.

Buick, I. S., Hermann, J., Williams, I. S., Gibson, R. & Rubatto, D. 2006. A SHRIMP U–Pb and LA-ICP570 MS trace element study of the petrogenesis of garnet–cordierite–orthoamphibole gneisses from the Central Zone of the Limpopo Belt, South Africa. *Lithos* **88**, 150–72.

Caggianelli, A., Del Moro, A., Paglionico, A., Piccarreta, G., Pinarelli, L. & Rottura, A. 1991. Lower crustal genesis connected with chemical fractionation in the continental crust of Calabria (Southern Italy). *European Journal of Mineralogy* **3**, 159–80.

Caggianelli, A., Prosser, G. & Rottura, A. 2000. Thermal history vs. fabric anisotropy in granitoids emplaced at different crustal levels: an example from Calabria, southern Italy. *Terra Nova* **12**, 109–16.

Chen, R. X., Zheng, Y. F. & Xie, L. 2010. Metamorphic growth and recrystallization of zircon: Distinction by simultaneous in-situ analyses of trace elements, U-Th-Pb and Lu-Hf isotopes in zircons from eclogite-facies rocks in the Sulu orogen. *Lithos* **114**, 132–54.

Duchene, S., Fornelli, A., Micheletti, F. & Piccarreta, G. 2013. Sm-Nd chronology of porphyroblastic garnets from granulite facies metabasic rocks in Calabria (Southern Italy): inferences for preserved isotopic memory and resetting. *Mineralogy and Petrology* **107**(4), 539–51.

Fornelli, A., Langone, A., Micheletti, F., Pascazio, A. & Piccarreta, G. 2014. The role of trace element partitioning between garnet, zircon and orthopyroxene on the interpretation of zircon U–Pb ages: an example from high-grade basement in Calabria (Southern Italy). *International Journal of Earth Sciences* **103**(2), 487–507.

Fornelli, A., Langone, A., Micheletti, F. & Piccarreta, G. 2012. Application of U-Pb dating and chemistry of zircon in the continental crust of Calabria (Southern Italy). In *Zircon and Olivine: Characteristics, Types and Uses* (eds G. Van Dijk, V. Van den Berg), pp. 1–36. New York: Nova Science Publishers.

Fornelli, A., Langone, A., Micheletti, F. & Piccarreta, G. 2011. Time and duration of Variscan high-temperature metamorphic processes in the south European Variscides. Constraints from U-Pb chronology and trace–element chemistry of zircon. *Mineralogy and Petrology* **103**, 101–22.

Fornelli, A., Pascazio, A. & Piccarreta, G. 2011. Diachronic and different metamorphic evolution in the fossil Variscan lower crust of Calabria. *International Journal of Earth Sciences* **101**(5), 1191–207.

Fornelli, A., Piccarreta, G., Acquafredda, P., Micheletti, F. & Paglionico, A. 2004. Geochemical fractionation in migmatitic rocks from Serre Granulitic Terrane (Calabria, southern Italy). In Special Issue 2: A showcase of the Italian research in metamorphic petrology. *Periodico di Mineralogia* **73**, 145–57.

Fornelli, A., Piccarreta, G., Del Moro, A. & Acquafredda, P. 2002. Multi-stage melting in the Lower Crust of the Serre (Southern Italy). *Journal of Petrology* **43**(12), 2191–217.

Griffin, B. J., Joy, D. C. & Michael, J. R. 2010. A comparison of a luminescence-based VPSE and an electron-based GSED for SE and CL imaging in variable pressure SEM with conventional SE imaging. *Microscope Microanalyses* **16** (Suppl. 2), 624–5.

Harley, S. L. & Kelly, N. M. 2007. The impact of zircon-garnet REE distribution data on the interpretation of zircon U–Pb ages in complex high-grade terrains: an example from the Rauer Islands, East Antartica. *Chemical Geology* **241**, 62–87.

Harley, S. L., Kinny, P. D., Snape, I. & Black, L. P. 2001. Zircon chemistry and the definition of events in Archaean granulite terrains. In *Extended Abstracts of 4th International Archaean Symposium* (eds K. F. Cassidy, J. M. Dunphy and M. J. van Kranendonk), pp. 511–3. Canberra: AGSO Geoscience Australia Record 2001/37.

Hermann, J. & Rubatto, D. 2003. Relating zircon and monazite domains to garnet growth zones: age and duration of granulite facies metamorphism in the Val Malenco lower crust. *Journal of Metamorphic Geology* **21**(9), 833–52.

Hokada, T. & Harley, S. L. 2004. Zircon growth in UHT leucosome: constraints from zircon-garnet rare earth elements (REE) relations in Napier Complex, East Antarctica. *Journal of Mineralogical and Petrological Sciences*, **99**(4), 180–90.

Horn, I., Rudnik, R. L. & McDonough, W. F. 2000. Precise elemental and isotope ratio determination by simultaneous solution nebulization and laser ablation-ICP-MS: application to U–Pb geochronology. *Chemical Geology* **164**, 281–301.

Horstwood, M. S. A., Foster, G. L., Parrish, R. R., Noble, S. R. & Nowell, G. M. 2003. Common-Pb corrected in situ U–Pb accessory mineral geochronology by LA–MC–ICP–MS. *Journal of Analytical Atomic Spectrometry* **18**, 837–46.

Kelly, N. M. & Harley, S. L. 2005. An integrated microtextural and chemical approach to zircon geochronology: refining the Archaean history of the Napier Complex, east Antarctica. *Contributions to Mineralogy and Petrology* **149**(1), 57–84.

Ketchum, J. W. F., Jackson, S. E., Culshaw, N. G. & Barr, S. M. 2001. Depositional and tectonic setting of the Paleo-proterozoic Lower Aillik Group, Makkovik Province, Canada: evolution of a passive margin-foredeep sequence based on petrochemistry and U–Pb (TIMS and LAM-ICP-MS) geochronology. *Precambrian Research* **105**, 331–56.

Kretz, R. 1983. Symbols for rock-forming minerals. *American Mineralogist* **68**, 277–9.

Ludwig, K. 2003. *User's Manual for a Geochronological Toolkit for Microsoft Excel*. Berkeley Geochronology Center, Special Publication no. **4**, 53 pp.

Maccarrone, E., Paglionico, A., Piccarreta, G. & Rottura, A. 1983. Granulite–amphibolite facies metasediments from the Serre (Calabria, Southern Italy): their protoliths and the processes controlling their chemistry. *Lithos* **16**, 95–111.

McDonough, W. F. & Sun, S. S. 1995. The composition of the Earth. *Chemical Geology* **120**, 223–53.

Micheletti, F., Barbey, P., Fornelli, A., Piccarreta, G. & Deloule, E. 2007. Latest Precambrian to Early Cambrian U-Pb zircon ages of augen gneisses from Calabria (Italy), with inference to the Alboran microplate in the evolution of the peri-Gondwana terranes. *International Journal of Earth Sciences* **96**(5), 843–60.

Micheletti, F., Fornelli, A., Piccarreta, G., Barbey, P. & Tiepolo, M. 2008. The basement of Calabria (southern Italy) within the context of the Southern European Variscides: LA-ICPMS and SIMS U-Pb zircon study. *Lithos* **104**, 1–11.

Paglionico, A. & Piccarreta, G. 1976. Le Unità del Fiume Pomo e di Castagna nelle Serre Settentrionali (Calabria). *Bollettino della Società Geologica Italiana* **95**, 27–37.

Paglionico, A. & Piccarreta, G. 1978. History and petrology of a fragment of the deep crust in the Serre (Calabria, Italy). *Neues Jahrbuch für Mineralogie-Abhandlungen* (Journal of Mineralogy and Geochemistry) **9**, 385–96.

Rubatto, D. 2002. Zircon trace element geochemistry: partitioning with garnet and the link between U–Pb ages and metamorphism. *Chemical Geology* **184**, 123–38.

Rubatto, D. & Hermann, J. 2007. Experimental zircon/melt and zircon/garnet trace element partitioning and implications for the geochronology of crustal rocks. *Chemical Geology* **241**, 62–87.

Schenk, V. 1980. U-Pb and Rb-Sr radiometric dates and their correlation with metamorphic events in the granulite-facies basement of the Serre, southern Calabria (Italy). *Contributions to Mineralogy and Petrology* **73**, 23–38.

Schenk, V. 1984. Petrology of felsic granulites, metapelites, metabasics, ultramafics, and metacarbonates from Southern Calabria (Italy): prograde metamorphism, uplift and cooling of a former lower crust. *Journal of Petrology* **25**, 255–98.

Schenk, V. 1989. P-T-t path of the lower crust in the Hercynian fold belt of southern Calabria. In *Evolution of Metamorphic Belts* (eds J. S. Daly, R. A. Cliff & B. W. D. Yardley), pp. 337–42. Geological Society of London, Special Publication no. 43.

Skublov, S. & Drugova, G. 2003. Patterns of trace-element distribution in calcic amphiboles as a function of metamorphic grade. *The Canadian Mineralogist* **41**(2), 383–92.

Storkey, A. C., Hermann, J., Hand, M. & Buick, I. S. 2005. Using in situ trace-element determinations to monitor partial-melting processes in metabasites, *Journal of Petrology* **46**(6), 1283–308.

Tajcmanova, L., Podladchikov, Y., Powell, R., Moulas, E., Vrijmoed, J. C. & Connolly, J. A. D. 2014. Grain-scale pressure variations and chemical equilibrium in high-grade metamorphic rocks. *Journal of Metamorphic Geology* **32**, 195–207.

Taylor, R. J. M., Harley, S. L., Hinton, R. W., Elphick, S., Clark, C. & Kelly, N. M. 2015. Experimental determination of REE partition coefficient between zircon, garnet and melt: a key to understanding high-T crustal processes. *Journal of Metamorphic Geology* **33**, 231–48.

Tiepolo, M. 2003. In situ Pb geochronology of zircon with laser ablation inductively coupled plasma-sector field mass spectrometry. *Chemical Geology* **199**, 159–77.

Tiepolo, M., Bottazzi, P., Palenzona, M. & Vannucci, R. 2002. A laser probe coupled with ICP–double-focusing sector–field mass spectrometer for in situ analysis of geological samples and U–Pb dating of zircon. *Canadian Mineralogist* **41**, 259–72.

Trail, D., Watson, E. B. & Tailby, N. D. 2012. Ce and Eu anomalies in zircon as proxies for the oxidation state of magmas. *Geochimica et Cosmochimica Acta*, **97**, 70–87.

van Achterbergh, E., Ryan, C., Jackson, S. & Griffin, W. 2001. Data reduction software for LAICPMS. In *Laser Ablation ICPMS in the Earth Science Principles and Application* (ed. P. Sylvester), pp. 239–43. Mineralogical Association of Canada, Short Course no. 29.

Whitehouse, M. J. & Platt, J. P. 2003. Dating high-grade metamorphism: constraints from rare-earth 675 elements in zircon and garnet. *Contribution to Mineralogy and Petrology* **145**, 61–74.

Wiedenbeck, M., Allé, P., Corfu, F., Griffin, W. L., Meier, M., Oberli, F., Von Quadt, A., Roddick, J. C. & Spiegel, W. 1995. Three natural zircon standards for U–Th–Pb, Lu–Hf, trace elements and REE analyses. *Geostandards Newsletter* **19**, 1–23.

Xia, X. Q., Zheng, Y. F., Yuan, H. & Wu, F. Y. 2009. Contrasting Lu–Hf and U–Th–Pb isotope systematics between metamorphic growth and recrystallization of zircon from eclogite-facies metagranites in the Dabie orogen, China. *Lithos* **112**, 477–96.

Zhang, S. B., Zheng, Y. F. & Zhao, Z. F. 2010. Temperature effect over garnet effect on uptake of trace elements in zircon of TTG-like rocks. *Chemical Geology* **274**, 108–25.

Zhou, L. G., Xia, X. Q., Zheng, Y. F. & Chen, R. X. 2011. Multistage growth of garnet in ultrahigh-pressure eclogite during continental collision in the Dabie orogen: constrained by trace elements and U-Pb ages. *Lithos* **127**, 101–27.

Zong, K., Liu, Y., Gao, C., Hu, Z., Gao, S. & Gong, H. 2010. In situ U-Pb dating and trace element analysis of zircons in thin sections of eclogite: refining constraints on the ultra high-pressure metamorphism of the Sulu terrane, China. *Chemical Geology* **269**, 237–51.

https://doi.org/10.1017/S001675681700067X Published online by Cambridge University Press